

RESEARCH

Open Access



A loss-of-function mutation in human *Oxidation Resistance 1* disrupts the spatial–temporal regulation of histone arginine methylation in neurodevelopment

Xiaolin Lin^{1,2,3,4}, Wei Wang³, Mingyi Yang^{1,2,4,5}, Nadirah Damseh⁶, Mirta Mittelstedt Leal de Sousa³, Fadi Jacob⁷, Anna Lång^{1,2}, Elise Kristiansen^{1,4}, Marco Pannone³, Miroslava Kissova³, Runar Almaas⁸, Anna Kuśnierczyk^{1,9}, Richard Siller^{5,10}, Maher Shahrour^{6,11}, Motee Al-Ashhab⁶, Bassam Abu-Libdeh⁶, Wannan Tang³, Geir Slupphaug^{1,9}, Orly Elpeleg¹², Stig Ove Bøe^{1,2}, Lars Eide², Gareth J. Sullivan^{5,10,13}, Johan Egge Rinholm^{1,9}, Hongjun Song⁷, Guo-li Ming⁷, Barbara van Loon³, Simon Edvardson^{12*}, Jing Ye^{3*} and Magnar Bjørås^{1,2,3,4,5*} 

*Correspondence: SIMON@hadassah.org.il; jing.ye@ntnu.no; Magnar.Bjoras@ntnu.no

¹ Department of Microbiology, Oslo University Hospital and University of Oslo, Oslo, Norway

³ Department of Clinical and Molecular Medicine (IKOM), Norwegian University of Science and Technology (NTNU), 7491 Trondheim, Norway

¹² Department of Genetics, Hadassah University Hospital, Jerusalem, Israel

Full list of author information is available at the end of the article

Abstract

Background: *Oxidation Resistance 1 (OXR1)* gene is a highly conserved gene of the TLDc domain-containing family. OXR1 is involved in fundamental biological and cellular processes, including DNA damage response, antioxidant pathways, cell cycle, neuronal protection, and arginine methylation. In 2019, five patients from three families carrying four biallelic loss-of-function variants in OXR1 were reported to be associated with cerebellar atrophy. However, the impact of OXR1 on cellular functions and molecular mechanisms in the human brain is largely unknown. Notably, no human disease models are available to explore the pathological impact of OXR1 deficiency.

Results: We report a novel loss-of-function mutation in the TLDc domain of the human *OXR1* gene, resulting in early-onset epilepsy, developmental delay, cognitive disabilities, and cerebellar atrophy. Patient lymphoblasts show impaired cell survival, proliferation, and hypersensitivity to oxidative stress. These phenotypes are rescued by TLDc domain replacement. We generate patient-derived induced pluripotent stem cells (iPSCs) revealing impaired neural differentiation along with dysregulation of genes essential for neurodevelopment. We identify that OXR1 influences histone arginine methylation by activating protein arginine methyltransferases (PRMTs), suggesting OXR1-dependent mechanisms regulating gene expression during neurodevelopment. We model the function of OXR1 in early human brain development using patient-derived brain organoids revealing that OXR1 contributes to the spatial–temporal regulation of histone arginine methylation in specific brain regions.

Conclusions: This study provides new insights into pathological features and molecular underpinnings associated with OXR1 deficiency in patients.



© The Author(s) 2023. **Open Access** This article is licensed under a Creative Commons Attribution 4.0 International License, which permits use, sharing, adaptation, distribution and reproduction in any medium or format, as long as you give appropriate credit to the original author(s) and the source, provide a link to the Creative Commons licence, and indicate if changes were made. The images or other third party material in this article are included in the article's Creative Commons licence, unless indicated otherwise in a credit line to the material. If material is not included in the article's Creative Commons licence and your intended use is not permitted by statutory regulation or exceeds the permitted use, you will need to obtain permission directly from the copyright holder. To view a copy of this licence, visit <http://creativecommons.org/licenses/by/4.0/>. The Creative Commons Public Domain Dedication waiver (<http://creativecommons.org/publicdomain/zero/1.0/>) applies to the data made available in this article, unless otherwise stated in a credit line to the data.

Keywords: *Oxidation Resistance 1* (OXR1), Induced pluripotent stem cells (iPSCs), Brain organoids, Neurodevelopmental disorder, Protein arginine methyltransferases (PRMTs), Histone arginine methylation

Background

Oxidation Resistance 1 (OXR1, HGNC: 15,822, alias: *TLDC3*) is a highly conserved gene of the TLDC domain-containing family [1–6], first reported in *Escherichia coli* in 2000 [7] and then confirmed in almost all eukaryotes [3]. OXR1 plays an essential role in oxidative stress resistance [3–20], but not directly in reactive oxygen species (ROS) scavenging [12] nor possessing catalase or superoxide dismutase activity [13]. It is involved in fundamental cellular and biological processes including DNA damage response [7, 8, 14], antioxidant pathways [14, 21], cell cycle [14, 15, 22], mitochondrial functions [8, 14, 16], glucose metabolism [23], S-nitrosylation [5], V-ATPase regulation [24], lysosomal functions [4], immune defense [25, 26], inflammatory response [18, 27], neuronal protection [3–5, 12, 17–20, 28], and life-span [13, 29]. It is associated with a wide range of diseases, such as amyotrophic lateral sclerosis (ALS) [3, 17–19], Parkinson's disease [20], retinopathy [30, 31], and Lupus nephritis [27], pulmonary arterial hypertension [21], etc. [21, 32, 33].

Due to the importance of ROS as signaling molecules in the brain, the high metabolic rate, and a relatively low antioxidant capacity, the brain is assumed to be particularly susceptible to an imbalance in ROS levels [34]. *Oxr1*-depleted mice display progressive cerebellar ataxia, shortened lifespan, and confers neuronal sensitivity to oxidative stress [5, 12]. Overexpression of *Oxr1* in variant ALS mouse models delayed the onset of neuromuscular phenotypes and neuroinflammatory responses and improved motor neuron functions [17–19]. A systemic analysis of mammal TLDC domain-containing proteins showed *Oxr1* was highly expressed in the central nervous system of mice, and disruptions of the TLDC domain in *Oxr1* caused neurodegeneration [3]. In addition to the C-terminal TLDC domain, *Oxr1* long isoforms also contain the evolutionarily conserved Tre2/Bub2/Cdc16 (TBC) domain and Lysin Motif (LysM) [3]. However, the structural or functional roles of these domains remain elusive.

In 2019, it was reported that five patients from three families who carried four biallelic loss-of-function OXR1 variants were associated with cerebellar atrophy [4]. The impact of OXR1 deficiency was further assessed in *Drosophila* models. Complete deletion of the *mustard* (*mtd*) gene, the fly homolog of human OXR1 and NCOA7, was lethal, which was rescued by the replacement of human OXR1 cDNA (TLDC domain only). In addition, neuron-specific depletion of *mtd* in flies led to an accumulation of aberrant lysosomal structures, massive neuronal loss, and early death [4]. However, no human disease models are available to explore the pathological impact of OXR1 deficiency in the brain. The role of OXR1 in cellular functions and molecular mechanisms remains largely unknown.

Here, we characterized a novel and deleterious OXR1 mutation in patients with severe neurological features. We produced patient-derived lymphoblasts, fibroblasts, iPSCs, and used the latter to generate monolayer neuronal cell cultures and various brain organoid models (e.g., hippocampus, hypothalamus, midbrain, and forebrain) to systematically analyze key aspects of the pathological features and molecular mechanisms

associated with OXR1 depletion in human. We found that the pathological phenotypes in patient lymphoblasts, such as impaired cell survival, proliferation, and hypersensitivity to oxidative stress, were rescued by the replacement of TLDC domain. In the patient derived iPSCs, impaired neural differentiation along with dysregulation of genes essential for neurodevelopment was identified. Further, we demonstrated that OXR1 influenced histone arginine methylation by activating protein arginine methyltransferases and revealed that OXR1 contributed to the spatial–temporal regulation of histone arginine methylation during human brain development.

Results

Characterization of OXR1 deficiency and description of clinical phenotypes

Three sisters whose parents were first cousins (Fig. 1a) presented delay or loss of developmental milestones after birth or at 8–10 months of age accompanied with focal myoclonic movement, hypoactivity, cognition problems, and frequent onset of epilepsy. Upon examination, patients showed non-communicative, generalized hypotonia, hyporeflexia/areflexia, ataxia and lack of spontaneous movements (Table 1). Electroencephalogram examination revealed generalized frank epileptic activity. Magnetic resonance imaging (MRI) disclosed atrophy particularly in vermis and cerebellum, and thin corpus callosum (Fig. 1b). To identify the genetic lesion responsible for these clinical features, we first performed exome sequencing of patient II-6. Exome analyses revealed that the homozygous variant Chr8:107,758,095 G > C at the donor splice site located at exon 18 of the *OXR1* gene (Hg19 chr8:g.107758095G > C, XM_005250993.1:c.2552 + 5G > C) segregated with the disease (Fig. 1c). This mutation was not present in any of the nearly 60,000 exomes deposited by the Exome Aggregation Consortium, Cambridge, MA (URL: <http://exac.broadinstitute.org>, accessed August 2016). The human *OXR1* gene consists of 19 exons (ENSG00000164830, GRCh38), resulting in at least 4 major isoforms, OXR1A–D, with different tissue distributions. For instance, OXR1A and OXR1D are expressed in human brain [14], whereas most other cell types express isoforms B and D. All isoforms contain the C-terminal TLDC domain. Sequencing cDNA of patient II-4 fibroblasts, the flanking *OXR1* exons 17–19 showed a shorter fragment (185 bp) compared to control cells (259 bp), indicative of homozygous skipping of exon 18 in *OXR1* (Fig. 1d, Additional file 1: Fig. S1a,b), predicted to cause a frameshift leading to loss of the highly conserved C-terminal 69 amino acids of the TLDC domain of all OXR1 isoforms. Western blot of control cells showed a strong band corresponding to the OXR1B protein that was absent in the patient cells (Fig. 1e), indicating that lack of exon 18 leads to protein instability. Therefore, it appears that the *OXR1* splicing mutation results in OXR1 depletion.

OXR1 deficiency compromises cell growth, survival, and response to oxidative stress in patient-derived lymphoblasts

To explore the functional impact of OXR1 deficiency in patients, we established lymphoblast cell lines (LB) from the patient (LB-*OXR1*^{ΔEx18}) and one unaffected sibling as control (LB-CTRL). The *OXR1* transcripts that were specific to the patients' exon skipping sequence (Exon 18) were largely reduced in LB-*OXR1*^{ΔEx18} whereas the *OXR1B* transcripts increased about 1.7 fold (Additional file 1: Fig. S1c). The LB-*OXR1*^{ΔEx18} showed

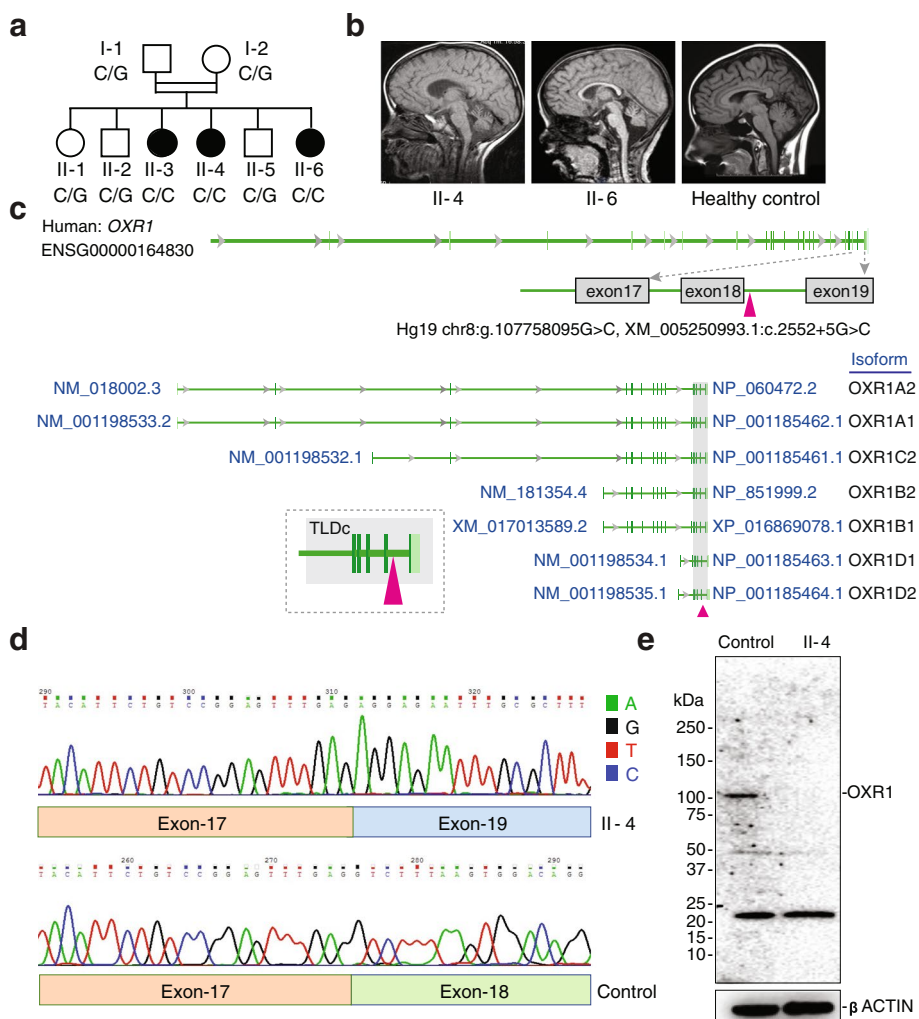


Fig. 1 Donor splice site mutation in the *OXR1* gene leads to exon skipping and protein depletion. **a** Family pedigree with genotype of Chr8:107,758,095 G > C mutation in the *OXR1* gene. **b** Brain MRI. Mid-sagittal T1 weighted images showing marked cerebellar atrophy in patient II- 4 at 6 years (left) and patient II-6 at 3 years and 4 months (middle), compared with the same view of a healthy control at 6-years (right). **c** Genomic structure of human *OXR1* and the mutation site. The *OXR1* gene is located on chromosome 8 and consists of 19 exons, reference to ENSG000001164830 (Hg19). Triangle in magenta, the mutation in the donor splicing site of exon 18 within TLDC domain (*OXR1*^{ΔEx18}), affecting all identified human *OXR1* isoforms. **d** cDNA sequence around the *OXR1* mutation site of lymphoblasts from patient II-4 and healthy control. **e** Western blot analysis of *OXR1* level in lymphoblasts from patient II-4 and healthy control. β-actin was used as loading control

reduced proliferation (Fig. 2a), higher sensitivity to H₂O₂ with increased apoptosis and necrosis (Fig. 2b, Additional file 1: Fig. S2a). H₂O₂ treatment induced higher ROS levels in LB-*OXR1*^{ΔEx18} compared to control (Additional file 1: Fig. S2b). To determine the levels of oxidative DNA damage, we measured accumulation of 8-oxoguanine (8-oxoG) in genomic DNA [35]. Basal levels of 8-oxoG were similar in patient and controls, but increased 8-oxoG levels were observed in LB-*OXR1*^{ΔEx18} upon H₂O₂ exposure (Fig. 2c). Furthermore, we determined the rate of mitochondrial DNA (mtDNA) mutagenesis [36], showing elevated mutation frequencies in the D-loop and 12S regions of mtDNA in LB-*OXR1*^{ΔEx18} (Additional file 1: Fig. S2c). We have previously shown that *OXR1* upregulates the expression of antioxidant genes via the p21 signaling pathway in HeLa cells

Table 1 Clinical features of OXR1 deficiency patients

Individual	II-3	II-4	II-6
Inheritance pattern		Autosomal recessive inheritance	
Pregnancy/At birth		Normal (Self-reported)	
Age at symptom onset	Birth	8 months	10 months
Disease progress	No regression	Acute regression	Gradual regression
		Faltering growth	
		Mental retardation	
Clinical manifestations Physical examination	Global neurodevelopmental delay, more pronounced in fine motor, speech and social skill		
	Epilepsy (focal or myoclonic; refractory and frequent)		
	Hypotonia, Hyporeflexia		
	Gait ataxia, Difficulties with balance		
MRI	Vermis and cerebellar atrophy; Thin corpus callosum		
EEG	Paroxysmal sharp slow waves		
	No organomegaly		
	No malformation		
Important negative findings	Plasma lactate and urinary organic acids: normal		
	CSF analysis: normal		
	Vision was intact and fundoscopy: normal		

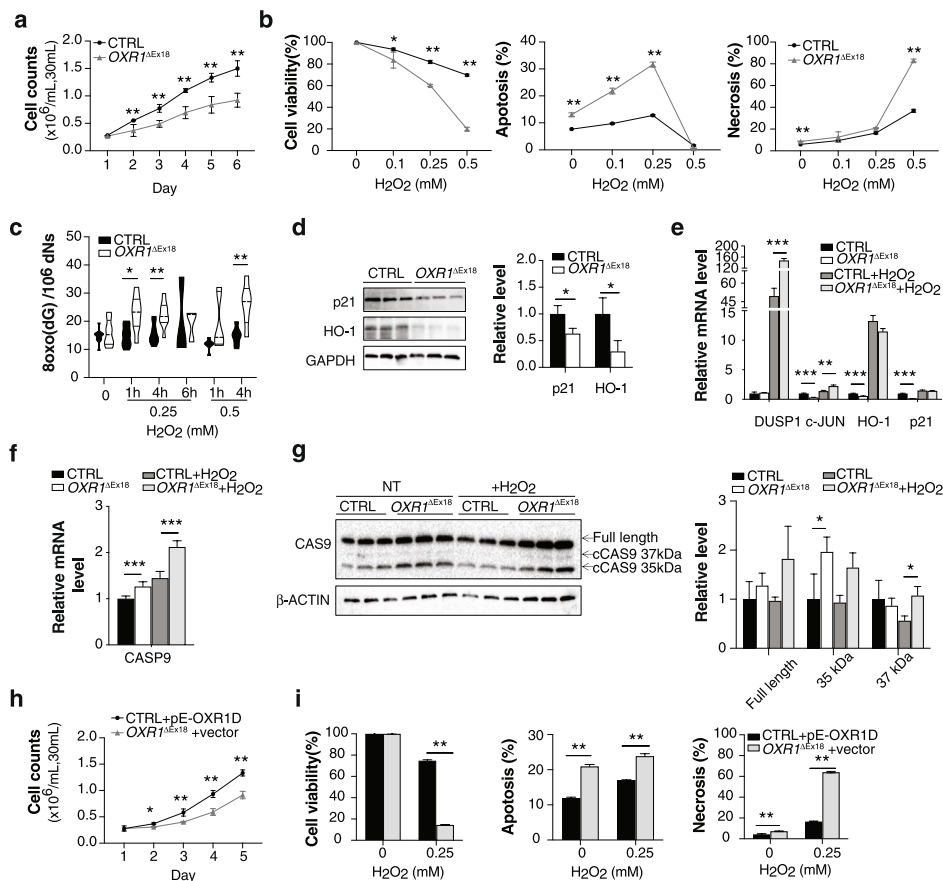


Fig. 2 OXR1 regulates cell proliferation, anti-oxidation response and apoptosis. **a** Proliferation capacity of patient ($OXR1^{\Delta Ex18}$) and control (CTRL) lymphoblasts. $n = 3$ independent experiments, $n = 6$ samples for each genotype in each experiment. **b** $OXR1^{\Delta Ex18}$ and CTRL lymphoblasts were treated with indicated concentrations of hydrogen peroxide (H_2O_2) for 1 h and harvested after 24 h recovery. Populations of surviving (left), apoptotic (middle) and necrotic (right) cells were determined by flow cytometry with FITC-Annexin V/PI double staining. $n = 3$ independent samples. **c** The detection of 8-oxoG levels in genomic DNA by mass spectrometry after H_2O_2 treatment in $OXR1^{\Delta Ex18}$ and CTRL lymphoblasts. $n = 3$ independent samples in the first assay (0.25 mM), and $n = 6$ independent samples in the second assay. **d** Western blot analysis and quantification of p21 and HO-1 expression under regular culturing conditions in $OXR1^{\Delta Ex18}$ and CTRL lymphoblasts. $n = 3$ independent samples. **e** Quantitative real-time PCR analysis of oxidative stress response genes in $OXR1^{\Delta Ex18}$ and CTRL lymphoblasts exposed to H_2O_2 and recovery for 6 h (R6h). $n = 3$ independent samples. **f** qPCR analysis of Caspase-9 (*CASP9*) expression in $OXR1^{\Delta Ex18}$ and CTRL lymphoblasts following 0.25 mM H_2O_2 treatment and recovery for 6 h (R6h). $n = 3$ independent samples. **g** Western blot analysis and quantification of CAS9 expression and cleaved CAS9 (cCAS9) in $OXR1^{\Delta Ex18}$ and CTRL lymphoblasts exposed to 0.25 mM H_2O_2 and recovery for 3 h (R3h) or non-treated (NT). β -ACTIN used as loading control, $n = 3$ independent samples. **h** Proliferation capacity of patient lymphoblasts with stable expression of OXR1D (LB- $OXR1^{\Delta Ex18}$ + pE-OXR1D) compared to patient lymphoblasts carrying only vector (LB- $OXR1^{\Delta Ex18}$ + vector), $n = 6$ independent samples. **i** Analyses of cell viability, apoptosis and necrosis patient lymphoblast samples stably expressing OXR1D (LB- $OXR1^{\Delta Ex18}$ + pE-OXR1D) or empty vector (LB- $OXR1^{\Delta Ex18}$ + vector) upon H_2O_2 treatment. $n = 3$ independent samples. All Data are shown as mean \pm SD. * $p < 0.05$, ** $p < 0.01$, multiple t test using the Holm-Sidak method to correct multiple comparisons when determining the statistical significance

[14]. In this study, we observed a reduction of both p21 and heme oxygenase (HO-1) proteins in LB- $OXR1^{\Delta Ex18}$ (Fig. 2d) and upregulation of stress response genes, including *DUSP1*, and the transcription factors (TF) *FOS* and *JUN* at the mRNA level (Fig. 2e, Additional file 1: Fig. S2d). ROS induced activation of caspases is pivotal in apoptosis.

Caspase-9 mRNA levels (Fig. 2f), as well as the activated forms of Caspase-9 (35 and 37 kDa) were significantly increased in LB-*OXR1*^{ΔEx18} (Fig. 2g). Taken together, these results demonstrate that *OXR1* deficiency reduces cell proliferation and increases intracellular oxidative stress, oxidative DNA damage and apoptosis.

The TLDc domain is essential for *OXR1*'s anti-oxidation function [3]. *OXR1D* is predominantly composed of the TLDc domain and is expressed in all types of tissues in human. To validate whether the observed cellular phenotypes were due to the mutation in the TLDc domain, we performed rescue experiments using LB-*OXR1*^{ΔEx18} cells stably expressing *OXR1D*-GFP. Strikingly, expression of *OXR1D*-GFP was sufficient to increase the proliferation capacity of LB-*OXR1*^{ΔEx18} (Fig. 2h) and reduced apoptosis and necrosis to levels comparable to control LBs (Fig. 2i). These results suggest that the splicing site mutation in TLDc domain leads to depletion of *OXR1* isoforms with loss-of-function.

Loss of *OXR1* causes morphological and developmental defects in neuronal cells

To overcome the challenge due to the lack of access to patient brain tissues for understanding the pathological mechanisms, we generated iPSCs from fibroblasts of patient II-4 and a healthy control (AG05836). Loss of exon18 was conserved, and the *OXR1* protein was absent in the patient iPSCs (Additional file 1: Fig. S3a,b). All control and *OXR1*^{ΔEx18} clones showed normal karyotypes, similar expression levels of pluripotency markers, and in vitro confirmation of pluripotency via directed differentiation to the three germ layers (Additional file 1: Fig. S3c-f, Additional file 2: Video S1). However, further differentiation of iPSCs into neurons revealed irregularities in the morphology of *OXR1*^{ΔEx18} neural aggregates (NAs) (Additional file 1: Fig. S3g,h). Moreover, *OXR1*-depletion reduced neurite growth (Fig. 3a), as well as the number of neurons, concomitant with reduced expression of neuronal markers, e.g., microtubule-associated protein 2 (MAP2) and class III beta-tubulin (Tuj1) (Additional file 1: Fig. S3i, j). Similar to patient LBs (Fig. 2b), *OXR1*-depleted neuronal cells displayed enhanced apoptosis (Additional file 1: Fig. S3k). Notably, *OXR1* mRNA and protein levels increased during neural differentiation in control cells (Additional file 1: Fig. S3l). Taken together, these results demonstrate an essential role of *OXR1* in neural differentiation.

OXR1 impacts transcription during neuronal differentiation

Previous work in our lab has demonstrated a role for *OXR1* in transcriptional regulation [1, 15]. To elucidate *OXR1*-dependent regulation of transcriptional networks during neural differentiation, the transcriptome analysis was performed at three distinct stages during neuronal differentiation (iPSCs, NAs and neurons) of control and *OXR1*^{ΔEx18} iPSCs (Additional file 1: Fig. S3i, m-t). Transcriptomes of three clones of control iPSCs, NAs and neurons showed distinct clustering, suggesting a well-defined, stage-specific neural differentiation process (Fig. 3b). In contrast, no prominent clustering was observed between the three groups of *OXR1*^{ΔEx18} cells. Significantly, the differentially expressed gene (DEG) population in *OXR1*^{ΔEx18} cells ($P_{adj} < 0.05$) had a steep increase of the median Log_2FC (fold change) from the iPSC stage (median $\text{Log}_2\text{FC} = 0.8276$, 95% CI 1.119–1.158), to the NA stage (median $\text{Log}_2\text{FC} = 1.069$, 95% CI 1.541–1.607), and to the neuron stage (median $\text{Log}_2\text{FC} = 1.342$, 95% CI 1.735–1.792) (Fig. 3c). With a threshold of $\text{Log}_2\text{FC} > |1.5|$, almost 3.5-fold more DEGs were identified at the neuron stage (3793

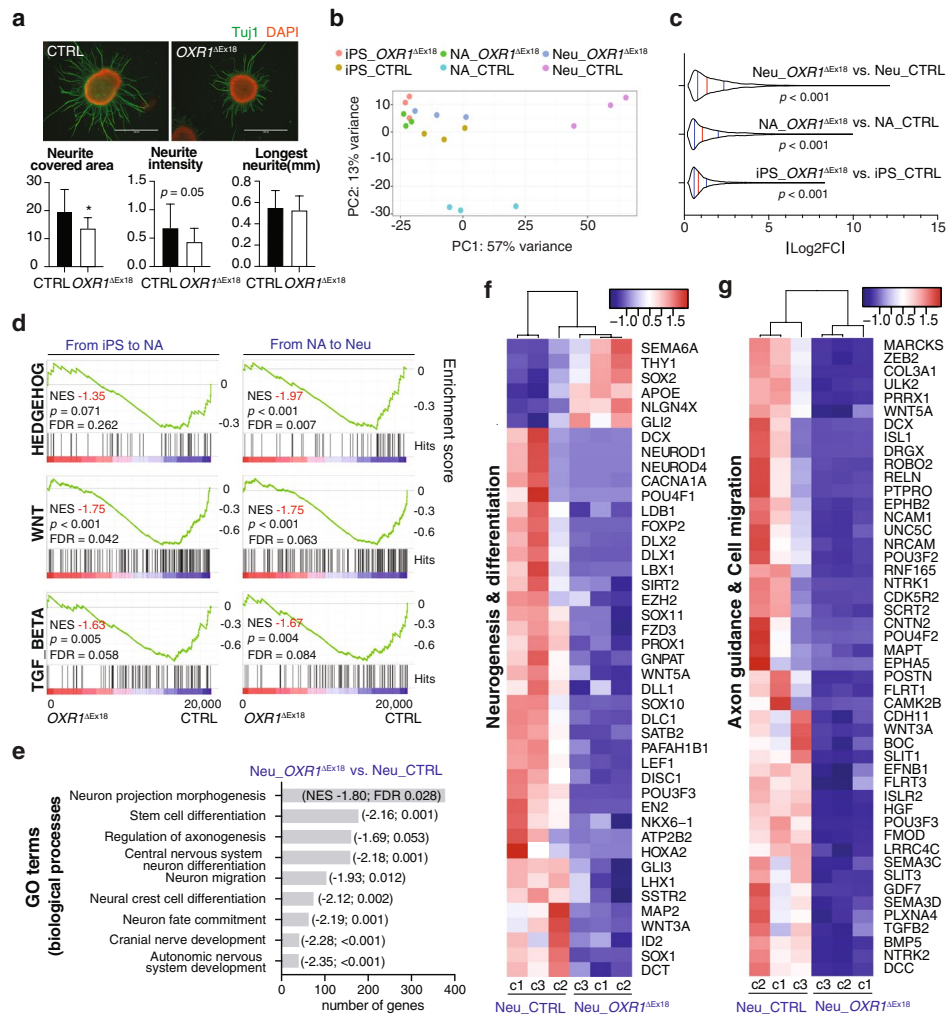


Fig. 3 OXR1 is required for planar neural differentiation. **a** Immunocytochemical analyses of neurospheres from patient (*OXR1^{ΔEx18}*) and healthy control (CTRL). Neurite outgrowth is visualized by antibody against neuron-specific class III beta-tubulin (Tuj1). Bar diagrams show quantification of the neurite (Tuj1+) covered area, the fluorescence intensity of covered area, and the longest neurite length by average of 5 longest neurites of each neurosphere ($n = 15$ independent neurospheres for each genotype). **b** Principal components analysis (PCA) showing the clustering of samples based on principal component 1 and 2 (PC1 and PC2). All samples are three different clones of each genotype derived from the monolayer neuronal differentiation experiment. Induced pluripotent stem cells (iPSC) were collected at day0, neural aggregates (NA) at day 2 (48 h after initiation of differentiation) and neurons (Neu) at day 20. **c** The violin plot shows the Log_2FC distribution of DEGs in patient (*OXR1^{ΔEx18}*) samples at each differentiation stage ($\text{Padj} < 0.05$). The median values were indicated by red lines, the quartiles were indicated by blue lines. The discrepancy was analyzed by Wilcoxon Signed Rank Test at 95% confidence interval. All p values < 0.001 . **d** Pathway enrichment analysis showing the core pathways involved in neural development by Gene Set Enrichment Analysis (GSEA, normalized enrichment score, $|\text{NES}| \geq 1$; nominal p value, ($p < 0.05$; false discovery rate ($\text{FDR} \leq 0.25$)). **e** Gene Ontology (GO) analysis by GSEA. The most underrepresented GO terms of biological processes in *OXR1^{ΔEx18}* neurons are relevant to neural development. The NES and FDR values were indicated next to each bar. **f** Heatmap showing z-score normalized read counts of the top ranked leading-edge genes in neurogenesis and differentiation that were differentially expressed in *Neu_OXR1^{ΔEx18}*. **g** Heatmap showing z-score normalized read counts of the top ranked leading-edge genes in axon genesis and cell migration that were differentially expressed in *Neu_OXR1^{ΔEx18}*.

DEGs, representing 12.8% of total genes) than at the initial iPSC stage (1089 DEGs, representing 3.5% of total genes) (Additional file 1: Fig. S3m). These results indicate that the impact of OXR1 on transcription is more pronounced at the neuron than the iPSC

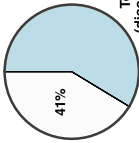
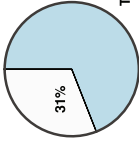
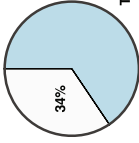
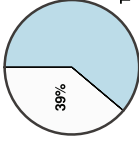
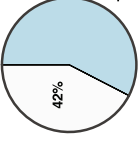
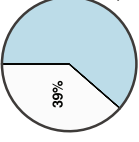
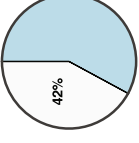
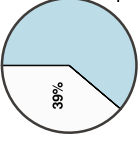
stage. Further, by searching published databases, we found that DEGs in patient-derived *OXR1*^{ΔEx18} neurons overlapped 39%, 41%, and 31% with disease-associated genes or high-confident risk genes of cerebellar atrophy, autism spectrum disorder, and schizophrenia, respectively (Table 2).

From iPSCs to neurons via NAs, lack of *OXR1* lead to progressive failure in neuron-fate commitment (Additional file 1: Fig. S3n), suggesting impaired neuronal differentiation trajectories upon *OXR1* depletion. Pathway enrichment by Gene Set Enrichment Analysis (GSEA) showed that the core pathways involved in neural development, such as Hedgehog, WNT, and TGF-beta, were activated in control, but not in *OXR1*^{ΔEx18} (Fig. 3d). Gene Ontology by GSEA revealed underrepresentation of biological processes required for the nervous system development, including hindbrain development (Fig. 3e, Additional file 1: Fig. S3p-q). Some overrepresented biological processes such as synaptic signaling and neurotransmitter transport were also identified (Additional file 1: Fig. S3o), indicating a potential role of *OXR1* in synaptic regulation. Genes essential for neurogenesis and neurodifferentiation as well as axon guidance and cell migration were significantly down-regulated in Neu-*OXR1*^{ΔEx18} (Fig. 3f-g). In addition, we found that several pro-apoptotic genes were upregulated while anti-apoptotic genes were down-regulated in Neu-*OXR1*^{ΔEx18} (Additional file 1: Fig. S3r), potentially contributing to the increased death of neurons (Additional file 1: Fig. S3k). Several oxidative stress response genes were upregulated (Additional file 1: Fig. S3s), supporting the oxidative distress in *OXR1*-depleted neurons, as observed in LB-*OXR1*^{ΔEx18}. According to a topologic biological network analysis of the dysregulated transcriptome of Neu-*OXR1*^{ΔEx18}, we found that *OXR1* orchestrated the expression of many key upstream regulators crucial for regulating transcription and substantial pathways for neural differentiation (Additional file 1: Fig. S3t). Further biological module clustering directly revealed *OXR1*-depletion impaired axon guidance at multiple levels, from axon genesis to neurite extension and synapse formation [37]. Among them, the dysregulated Reelin pathway, cell adhesion molecules (ie. *NRCAM*), Class-3 semaphorin, and Slit/Robo pathways were highlighted, which correlated to the formation of a thinner corpus callosum [38–40].

***OXR1* modulates PRMT-mediated histone modifications**

Next, we explored molecular mechanisms underlying *OXR1*-dependent regulation of gene expression. Previous mass spectrometry analysis revealed the interaction of over-expressed *OXR1*-GFP in U2OS cells with protein arginine methyltransferase 5 (PRMT5) [1], an epigenetic regulator of gene expression. Here, we confirmed the interaction of endogenous *OXR1* with PRMT5 as well as PRMT1 in U2OS cells by immunoprecipitation (IP) (Additional file 1: Fig. S4a), and in human fibroblasts (control vs *OXR1*^{ΔEx18}) by an *in-situ* proximity ligation assay (Fig. 4a). PRMTs can activate or repress gene expression by catalyzing histone (H) arginine (R) methylations on the N-terminus of histones H3 and H4, e.g., H3R2, H3R17, and H4R3 [41]. Crosstalk between histone arginine methylation and lysine acetylation/methylation has also been reported [42]. We examined histone modifications during the differentiation of iPSCs to neural stem cells (NSCs) using an antibody-based screening and revealed increased histone methylations on H3R2/R17, H4R3, H3K4/K9/K27 in the control NSCs (Fig. 4b). In contrast, *OXR1*-depleted NSCs showed significantly impaired histone arginine/lysine methylations, e.g.,

Table 2 Intersection-comparisons of OXR1 deficiency disease and other neurological developmental diseases

Disease	Autism spectrum disorder	Schizophrenia (risk)	Schizophrenia (high confidence risk)	Abnormal cerebellum morphology
				
Representation factor#	1.6	1.2	1.3	1.5
Probability#	$p < 1.717e-27$	$p < 2.126e-04$	$p < 5.632e-04$	$p < 8.366e-16$
Data resource	https://gene-archives.sifari.org/	N.A.	N.A.	https://hpo.jax.org/app/browse/term/HP:0001317
Pubmed References	PMID: 30545853/ 31974223	PMID: 29483656	PMID: 31974223/ 25056061	PMID: 27160001
Disease	Aplasia/Hypoplasia of the cerebellar vermis	Atrophy (wasting) of the cerebellum	Cerebellar dysplasia	Cerebellar hypoplasia/agenesis
				
Representation factor#	1.6	1.5	1.6	1.5
Probability#	$p < 3.107e-08$	$p < 3.177e-07$	$p < 0.092$	$p < 1.005e-06$
Data resource	https://hpo.jax.org/app/browse/term/HP:0006817	https://hpo.jax.org/app/browse/term/HP:0001272	https://hpo.jax.org/app/browse/term/HP:0007033	https://hpo.jax.org/app/browse/term/HP:0007360
Pubmed References	N.A.	PMID: 12169461	PMID: 25105227/ 27160001	PMID: 20305277

The representation factors and relevant probability are calculated by http://nemates.org/MA/progs/overlap_stats.html. All representation factors > 1

§ DEGs differentially expressed genes of Neu_OXR1^{ΔEx18} vs. Neu_CTRL

H3R2me2a, H3R17me2s/2a, H4R3me2s/2a, H3K4me3, H3K9me3, and H3K27me3. However, we did not detect any changes in the expression of PRMTs in either *OXR1*^{ΔEx18} iPSCs or NSCs as compared to control cells (Additional file 1: Fig. S4b). Thus, our results suggest that OXR1 may mainly affect the catalytic activity of PRMT-induced epigenetic histone modifications during neurogenesis.

To gain more insight into how OXR1 regulates histone marks, we integrated our RNA-sequencing data with published ChIP-sequencing datasets using the standard quality control available from <http://cistrome.org/db>. As shown in Fig. 4c, genes enriched with the repressive mark H4R3me2s overlapped with 71% of the down-regulated genes during neural differentiation in control cells (1319 out of 1869 genes), of which 63% of the genes were differentially expressed (up-regulated) in *OXR1*^{ΔEx18} cells (802 out of 1266 genes). Furthermore, genes enriched with H3K4me3, H3K9me3, H3K27me3, and H3K27ac overlapped with 16%-27% of the down- or up-regulated DEGs in *OXR1*^{ΔEx18} cells. These data may suggest a role of OXR1 in the regulation of histone modifications, particularly H4R3me2s.

To further explore a functional role of OXR1 in PRMT-catalyzed methylation of H4R3, we assessed the activity of the PRMT5/MEP50 methyltransferase on the Histone 4 N-terminal tail (aa1–21) in a methyltransferase assay in vitro by adding to the reactions full-length hOXR1A or mutant proteins with partial or complete deletion of TLDC (Fig. 4d). Interestingly, full-length hOXR1A and the mutants with partially truncated TLDC (*OXR1A_ΔTLDC_1*) stimulated PRMT5-catalyzed H4 methylation by threefold. In contrast, the *OXR1A* mutant lacking TLDC (*OXR1A_ΔTLDC_2*) failed to stimulate PRMT5 activity, suggesting the TLDC domain of OXR1 may have a role in the regulation of PRMT-catalyzed H4R3 methylation.

Impaired development of *OXR1* deficient human brain organoids

To unravel pathological processes at molecular, cellular, and structural levels, we modeled *OXR1* deficiency in the developing human brain organoids. We established cerebral organoids [43], and various brain region-specific organoids [44, 45] derived from patient iPSCs. Cerebral organoids often contain heterogeneous tissues resembling various brain regions, which relies on the intrinsic differentiation signaling and self-organization

(See figure on next page.)

Fig. 4 OXR1 modulates PRMT-induced epigenetic histone modifications during neurogenesis. **a** Proximity ligation assay showing the interaction of OXR1 with PRMT1 (magenta spots) and PRMT5 (green spots) in patient fibroblasts (*OXR1*^{ΔEx18}) and control cells (CTRL). Nuclei were indicated by DAPI staining. **b** The Western blot analysis showing histone arginine modifications in induced pluripotent stem cells (iPSC) and neural stem cells (NSC). The arginine modification marks include H3R2me2s, H3R2me2a, H3R17me2a, H4R3me2a, H4R3me2s, H3R17me2s, H3R26me2s, and lysine marks H3K4me3, H3K27me3, and H3K9me3; Histone 3 was used as loading control. **c** Overlay DEGs and putative targets of selected histone modifications in the published ChIPseq database. A representation factor (R) > 1 indicates more overlap than expected of two independent groups and a R < 1 indicates less overlap than expected. R = 1 indicates that the two groups by the number of genes expected for independent groups of genes. Probability (p) is indicated. Calculated by http://nemates.org/MA/progs/overlap_stats.cgi. **d** In vitro methyltransferase assay showing a direct role of OXR1 in regulating the enzymatic activity of PRMT5. N-terminal H4 peptides (1-21aa) and the mutant ones H4-R3K (1-21aa) were used as substrates. Different molar ratio of PRMT5/MEP50 protein complex (calculated as tetramer) to the full length OXR1A or truncated ones, such as 4:1 (+), 1:1(+ +), and 1:4(+ + +), was applied in each reaction. The enzymatic activity of PRMT5 was shown by the CPM (Count per minute) value of ³H-Methyl incorporation. All Data are shown as mean ± SD, **p* < 0.05, ****p* < 0.001, Student's *t* test

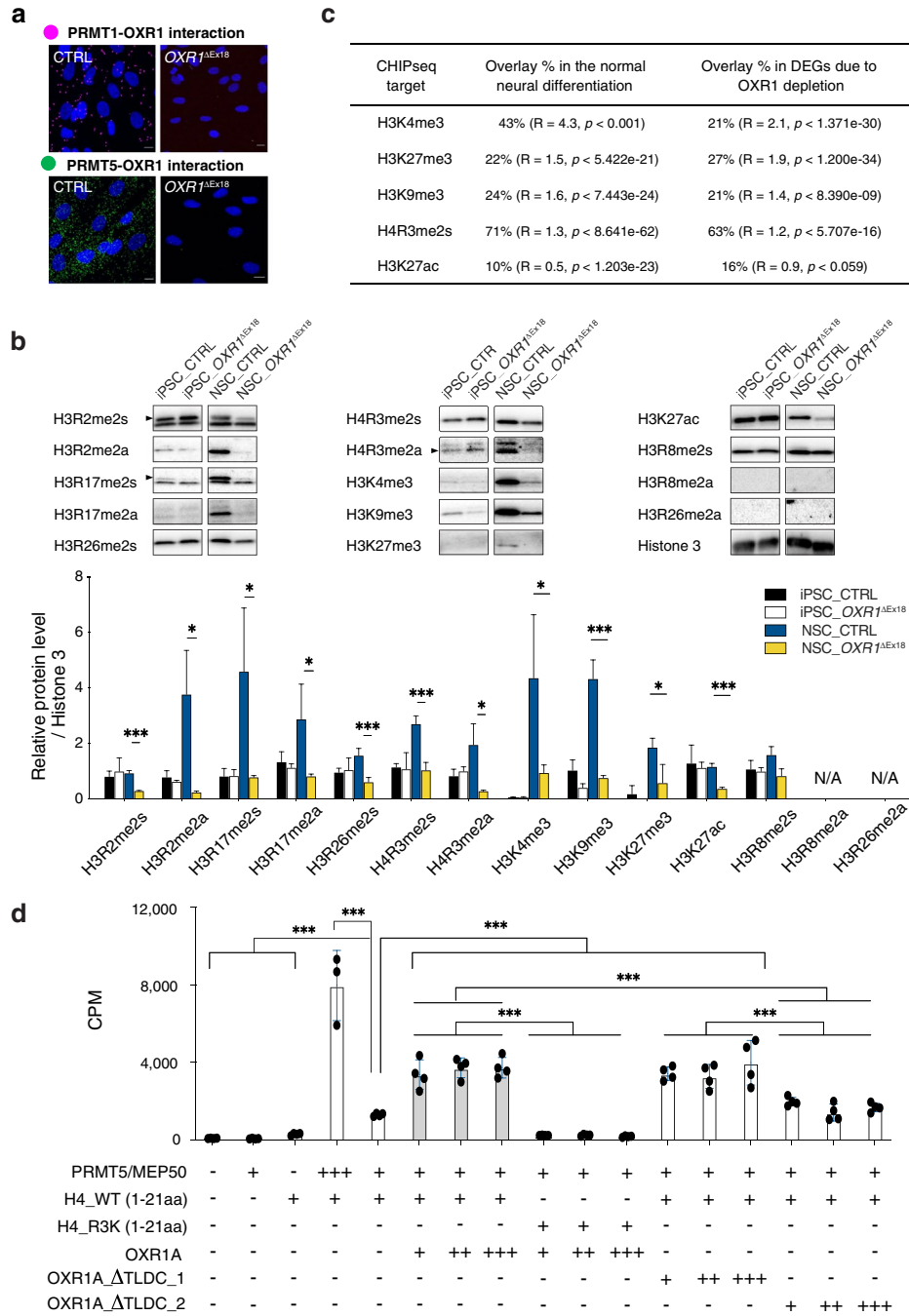


Fig. 4 (See legend on previous page.)

capacities of iPSCs (Fig. 5a). Significantly, *OXR1*^{ΔEx18} cerebral organoids were smaller than the healthy controls (CTRL) with slower growth rate and suboptimal morphology of neuroepithelial buds (Fig. 5a). After about 30 days, the cortical regions in healthy controls displayed dense and radially organized ventricular /subventricular zone (VZ/SVZ) like structures harboring the neural progenitor cells (NPCs). The neuronal layer composed of TBR1⁺ and CTIP2⁺ deep-layer neurons was highly reminiscent of the

formation of cortical plate (CP) (Additional file 1: Fig. S5a). New-born neurons continued to migrate radially outward, became mature (MAP2⁺) and obtained rudimentary separations during the lamination process (Fig. 5b). However, in *OXR1*^{ΔEx18} organoids, the two layers still intermingled at day 75 (Fig. 5b; Additional file 1: Fig. S5b), indicating either delayed neurogenesis or impaired neuron migration, or a combination. In addition, we observed a thick Reelin-positive (RELN⁺) layer along the basal surface reminiscent of the marginal zone with long and extended RELN⁺ plexus at the inner layer in control organoids at day75 (Fig. 5c; Additional file 1: Fig. S5c). It is known that RELN expressed at the marginal zone is essential for correct cortical and cerebellar neuronal lamination [46], and RELN localization along dendrites suggests a role in synaptic remodelling and neuronal maturation [47]. However, thinner marginal zone with reduced RELN deposition, shorten axons and lack of RELN⁺ plexus was observed in patient iPSC-derived organoids. These results suggest that *OXR1* deficiency leads to delayed neuronal layering in human cerebra.

OXR1^{ΔEx18} patients showed a global neurodevelopmental delay characterized by the dysfunctions of cognition, fine motor skills, learning and language, suggesting impaired functions not only in cerebellum, but also in cortical (i.e., prefrontal) areas and deep structures (i.e., hippocampus, basal ganglia). To assess the importance of *OXR1* in distinct brain regions, we guided neural progenitor cells (NPCs) to form brain region-specific identities by supplement of highly tailored external patterning factors at the early stage (Fig. 5d-h, 6a-c, 7a-d) [44, 48, 49]. From control iPSCs, we successfully generated hypothalamus, hippocampus, forebrain (cortical) and midbrain organoids with large VZ-like structures containing the region-specific NPCs. Molecular markers for cell identities were analyzed by IHC of different region-specific organoids. *OXR1* is highly expressed in both POMC⁺ peptidergic neurons and OTP⁺ hypothalamic neurons of hypothalamus organoids at day 50 (Additional file 1: Fig. S5d). Strikingly, *OXR1*-deficient clones from patient iPSCs lost the ability to form hypothalamus organoids (Fig. 5e). In addition, iPSC-*OXR1*^{ΔEx18} generated hippocampal organoids from only one clone (Fig. 5f) with a reduced size of SOX2-positive progenitor zone, a less organized layer of DCX-positive

(See figure on next page.)

Fig. 5 *OXR1* deficiency severely impairs brain development in distinct human brain organoid models. **a** The progression of cerebral organoid development is illustrated (upper). Representative bright-field images showing the progression of cerebral organoids derived from healthy control (CTRL) and patient (*OXR1*^{ΔEx18}) iPSC clones (lower left). Black arrows point the expanding neuroepithelial formation in CTRL clones from day 8 and the poorly developed neuroepithelia buds observed in the *OXR1*^{ΔEx18} cerebral organoids at day 15. The body size of cerebral organoids (lower right) is quantified by summing the products of bi-dimensional measurements (SPD). SPD = Longest diameter (LD) × longest diameter perpendicular to the LD. $n = 15-20$ organoids of each clone, * $p < 0.05$. **b** Immunohistochemical analyses of cerebral organoids at day 75 using the antibody specific for MAP2 (the marker of mature neurons, yellow) or TBR1 (the marker of deep layer neurons, magenta). **c** Immunohistochemical analyses of cerebral organoids at day 75 using antibodies specific for REELIN (yellow) and *OXR1* (magenta). **d** A schematic illustration showing the guided progression of region-specific brain organoids. **e** Representative bright-field images showing the progression of hypothalamus derived from CTRL and *OXR1*^{ΔEx18} iPSCs. The starting cell number of each clone is indicated (100% refer to 10,000 iPSC cells per microwell of Aggrewell-800 plate on day 0). After hypothalamus patterning, the spheroids of *OXR1*^{ΔEx18} clone 1 (c1) and *OXR1*^{ΔEx18} clone 2 (c2) dissipated by day 5. **f** Representative bright-field images showing the progression of hippocampus organoids. After hippocampus patterning, the spheroids of *OXR1*^{ΔEx18} c2 dissipated by day 5. **g** Representative confocal images showing the progression of SOX2⁺ neural progenitor cells (magenta) during the development of hippocampus organoids. **h** Representative confocal images showing the progression of NeuN⁺ mature neurons (grey) and DCX⁺ immature neurons (green) during the development of hippocampus organoids. In all confocal images, the scale bar is 60 μm and the nuclei were visualized using DAPI (blue)

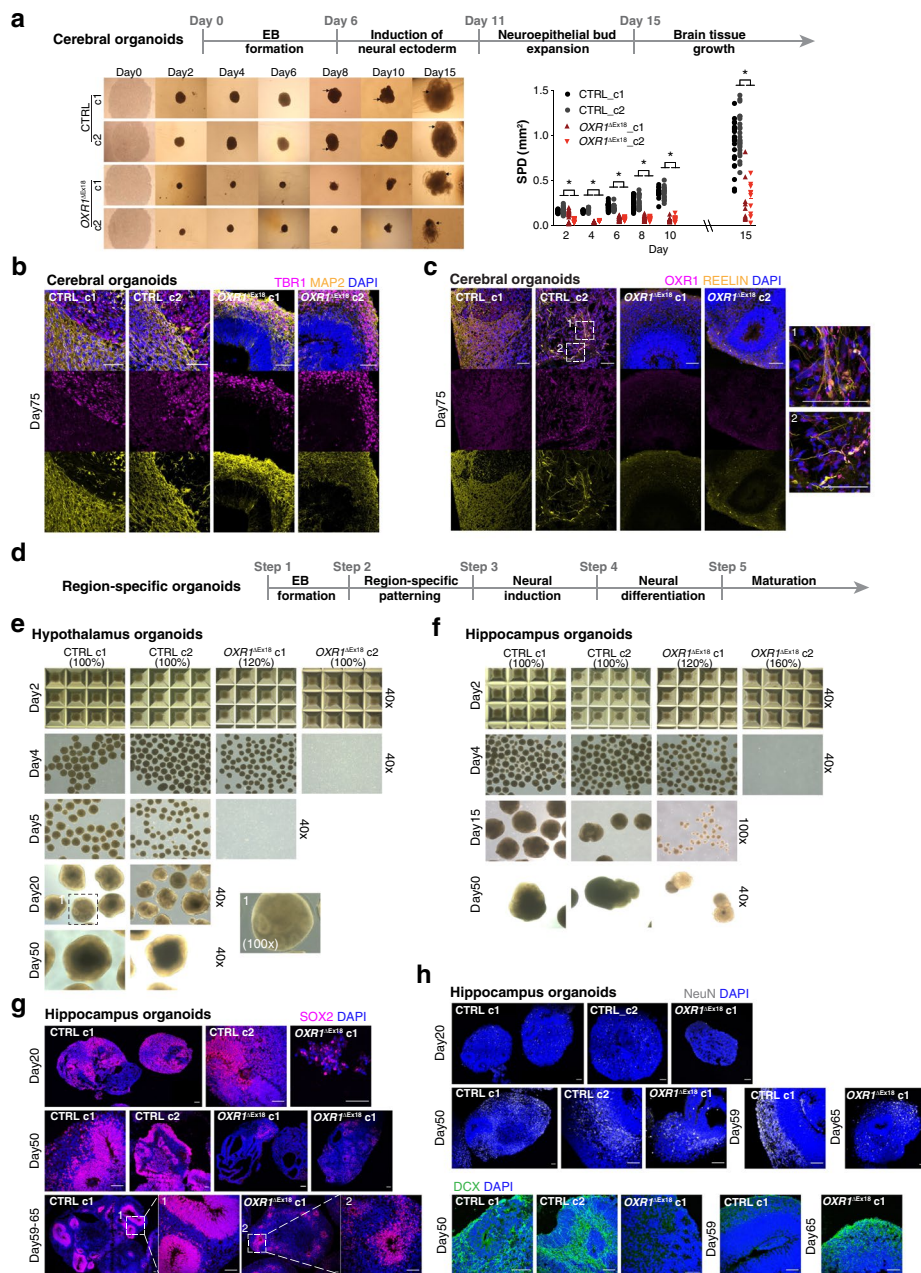


Fig. 5 (See legend on previous page.)

newborn neurons, and fewer NeuN-positive mature neurons (Fig. 5g-h; Additional file 1: Fig. S5e-f). Taken together, these results suggest a crucial role of OXR1 in early hypothalamus and hippocampal development.

OXR1 impacts early cortical development by shaping histone arginine methylations

We successfully generated cortical (forebrain) organoids from control and *OXR1*^{ΔEx18} iPSCs (Fig. 6a, Additional file 1: Fig. S6a). Control cortical organoids contained the large and radially organized VZ/SVZ like structures marked by SOX2 (Fig. 6b; Additional file 1: Fig. S6b), where cortical NPCs underwent active cell division (marked by Ki-67, in

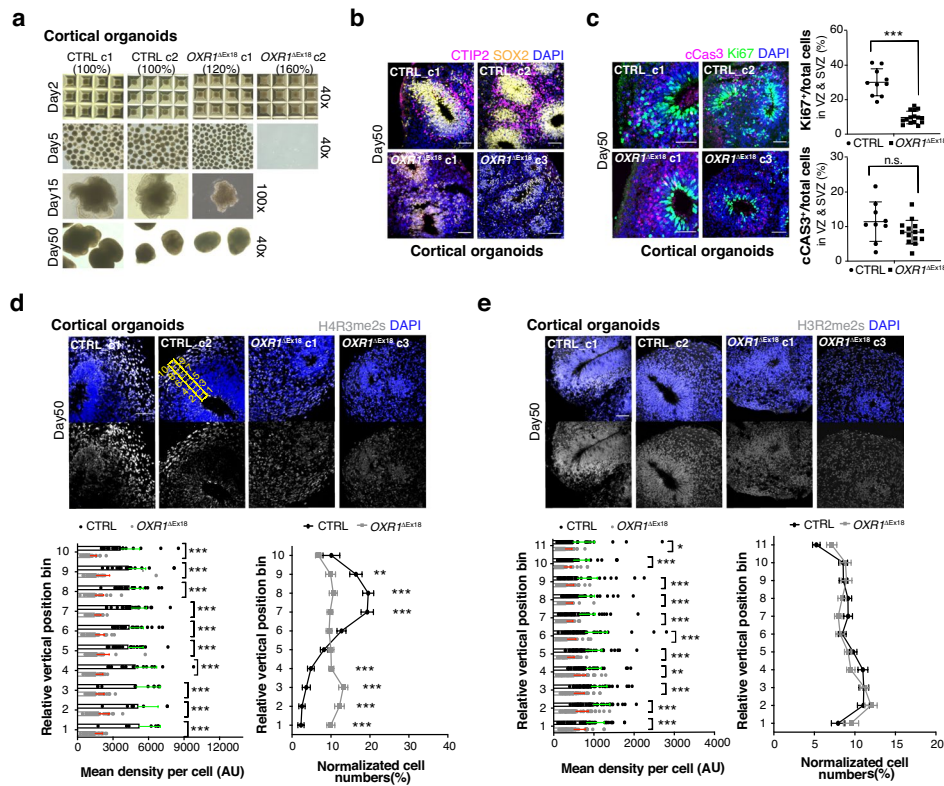


Fig. 6 OXR1 impacts cortical development by shaping histone arginine methylations. **a** Representative bright-field images (40x) showing the progression of cortical organoids, derived from CTRL and $OXR1^{\Delta Ex18}$ iPSCs. The starting cell number of each clone is indicated (100% refer to 10,000 iPSC cells per microwell of Aggrewell-800 plate on day 0). After cortical patterning, the spheroids of $OXR1^{\Delta Ex18}$ clone 2 (c2) usually dissipated by day 5. **b** Immunohistochemical analyses showing the CTIP2⁺ deep layer neurons (magenta) formed above SOX2-enriched progenitor zones (yellow) of cortical organoids at day 50. **c** Immunohistochemical analyses showing the Ki67⁺ proliferating cells (green) and cCas3⁺ apoptotic cells (magenta) at VZ/SVZ progenitor zones of cortical organoids at day 50. The bar diagram showing the percentage of Ki67⁺ or cCas3⁺ cells in VZ/SVZ. CTRL, $n = 10$; $OXR1^{\Delta Ex18}$, $n = 15$. VZ, ventricular zone; SVZ, subventricular zone. **d** Immunohistochemical analyses showing the distribution of H4R3me2s⁺ cells in cortical organoids at day 50. The average expression of H4R3me2s in each cell is quantified in each vertical position bin (yellow dash line). The normalized abundance of H4R3me2s⁺ cells in each vertical position bin was calculated as the number of H4R3me2s⁺ cells in a bin / the total number of H4R3me2s⁺ cells. CTRL, $n = 23$; $OXR1^{\Delta Ex18}$, $n = 26$ from two independent batches. **e** Immunohistochemical analyses showing the distribution of H3R2me2s⁺ cells of cortical organoids at day 50. The average expression of H4R3me2s of each cell was quantified in each vertical position bin (lower left). The normalized abundance of H3R2me2s⁺ cells in each vertical position bin was calculated as in (d). CTRL, $n = 49$; $OXR1^{\Delta Ex18}$, $n = 53$ from two independent batches. Values represent mean \pm SEM, * $p < 0.05$, ** $p < 0.01$, *** $p < 0.001$, Student's t test. In all confocal images, the scale bar is 60 μ m and the nuclei were visualized using DAPI (blue)

Fig. 6c). The newly generated layer of CTIP2⁺ early born neurons extended the formation of CP resembling human early corticogenesis (Fig. 6b). Interestingly, we identified a specific distribution of the histone arginine methylation mark H4R3me2s, which showed low levels in VZ/SVZ (including outer SVZ) like structures and increased levels in developing neurons outside the progenitor zone following the radial migration (Fig. 6d). This finding suggests a regulatory role of H4R3me2s during neurogenesis and the establishment of the cortical plate. However, the specific H4R3me2s distribution was affected in $OXR1^{\Delta Ex18}$ cortical organoids, showing an overall reduction of the H4R3me2s level (Fig. 6d). In addition, $OXR1^{\Delta Ex18}$ cortical organoids showed a thin and poorly organized

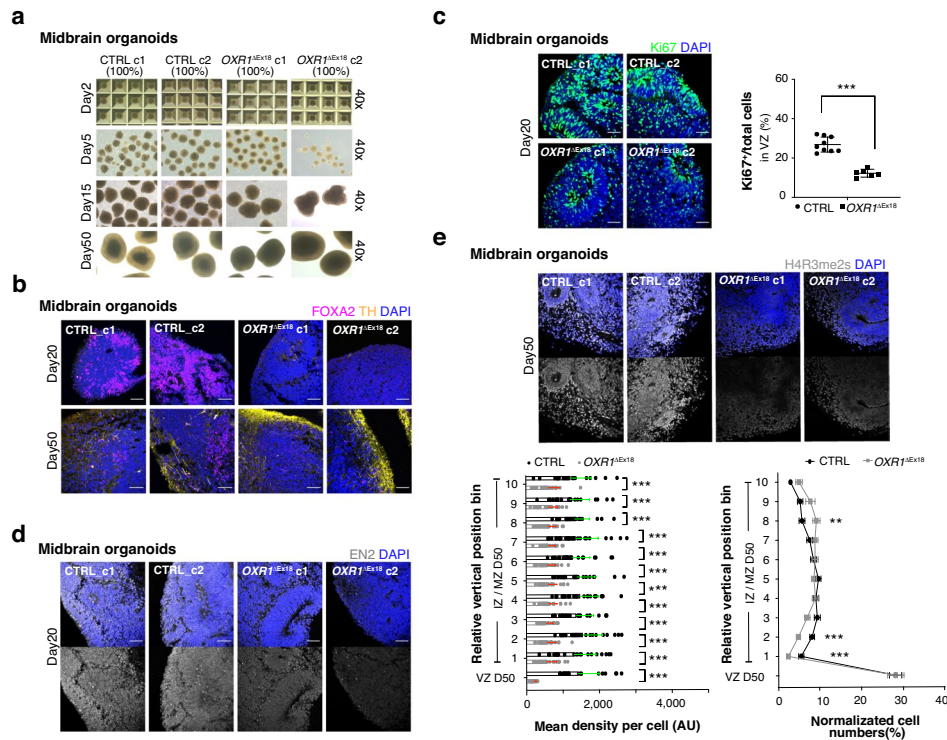


Fig. 7 OXR1 impacts midbrain development by shaping histone arginine methylations. **a** Representative bright-field images (40x) show the progression of midbrain organoids, derived from healthy control (CTRL) or and patient ($OXR1^{\Delta Ex18}$) iPSCs. The starting cell number of each clone is indicated (100% refer to 10,000 iPSC cells per microwell of Aggrewell-800 plate on day 0). After midbrain patterning, $OXR1^{\Delta Ex18}$ c2 showed less midbrain organoids generated at day 5. **b** Immunohistochemical analyses of midbrain organoids at day 20 and day 50 using antibodies specific for FOXA2 (magenta, the marker of midbrain floor plate/progenitor) and TH (yellow, the marker of dopaminergic neurons). **c** Immunohistochemical analyses showing $Ki67^+$ proliferating cells (green) in the VZ of midbrain organoids at day 20. The percentage of $Ki67^+$ cells in progenitor zones (VZ) was quantified. CTRL, $n = 9$ organoids; $OXR1^{\Delta Ex18}$, $n = 6$ organoids. **d** Immunohistochemical analyses showing transient expression of EN2 (the marker of mid-hindbrain boundary) in midbrain organoids at day 20. **e** Immunohistochemical analyses showing the spatial-temporal distribution of H4R3me2s in midbrain organoids at day 50. The average expression of H4R3me2s in each cell was quantified in each vertical position bin (lower left). The normalized abundance of H4R3me2s⁺ cells in each bin was calculated as in (Fig. 6d). CTRL, $n = 23$; $OXR1^{\Delta Ex18}$, $n = 23$ from two independent batches. Values represent mean \pm SEM, * $p < 0.05$, ** $p < 0.01$, *** $p < 0.001$, Student's *t* test. In all confocal images, the scale bar is 60 μ m and the nuclei were visualized using DAPI (blue)

VZ/SVZ with markedly reduced number of $Ki67^+$ proliferating NPCs, and a barely developed $CTIP2^+$ cortical plate (Fig. 6b, c). H3R2me2s, another target of PRMT5, displayed an even distribution pattern across the normal laminar cortical structures of control and $OXR1^{\Delta Ex18}$. However, an overall reduction of the H3R2me2s level was detected in $OXR1^{\Delta Ex18}$ cortical organoids (Fig. 6e). These results suggest that OXR1 impacts the early human corticogenesis by shaping histone arginine methylations.

OXR1 impacts early midbrain development by shaping histone arginine methylations

In addition, we generated midbrain organoids from control and $OXR1^{\Delta Ex18}$ iPSCs (Fig. 7a). Midbrain neurogenesis starts at VZ of the midbrain floor plate (mFP) where midbrain progenitors are differentiated into various types of tyrosine hydroxylase (TH⁺) midbrain dopaminergic (mDA) cells (Additional file 1: Fig. S6c). We guided midbrain

NPCs towards the identity of *substantia nigra pars compacta* (SNc) mDA neurons via the Shh-FOXA1/2-SOX6 pathway by using SHH, CHIR99021 and purmorphamine as patterning factors [37, 44, 50–56]. As expected, FOXA2⁺ progenitors were broadly detected at day 20, migrated through the intermediate zone (IZ) and became TH⁺ mDA when reaching mantle zone (MZ) at day 50 (Fig. 7b). In *OXR1*^{ΔEx18} midbrain organoids, FOXA2⁺ progenitors were sparsely detected at day 20 (Fig. 7b) with fewer Ki67⁺ proliferating midbrain NPCs (Fig. 7c), although the structural organization of VZ remained largely intact. In contrast, we observed an abnormal increase of TH⁺ mDA generated at day 50 (Fig. 7b), suggesting dysregulation of midbrain NPCs specification derived from the activation of FOXA2. It is known that upregulation of EN2 by FGF8 in the midbrain-hindbrain boundary is essential for further cerebellar development [57–59]. Similarly, EN2 was induced in VZ in control organoids, but absent in *OXR1*^{ΔEx18} (Fig. 7d), suggesting a potential mechanism underlying the cerebellar defects in patients. Notably, the distribution pattern of H4R3me2s in the control midbrain organoids was distinct from the cortical organoids by showing a high level in the VZ progenitor zone (Fig. 7e). Nevertheless, the level of H4R3me2s was dramatically decreased in *OXR1*^{ΔEx18} organoids. We did not detect any significant changes of H3R2me2a or H3R2me2s levels in *OXR1*^{ΔEx18} midbrain organoids (Additional file 1: Fig. S6d,e). But the distribution pattern and the expression level of histone lysine mark H3K4me3 were severely dysregulated in *OXR1*^{ΔEx18} midbrain organoids (Additional file 1: Fig. S6f). Taken together, these results suggest that OXR1 modulates distinct histone marks during early midbrain development, accounting for the clinical phenotypes in *OXR1*^{ΔEx18} patients.

Discussion

In this work, advanced human cell culture systems modeling OXR1 depletion provide new insight into the molecular and cellular pathology of rare diseases associated with inherited mutations of the TLDC containing family. We reported a de novo mutation within the critical TLDC domain of *OXR1* leading to exon skipping, protein depletion (*OXR1*^{ΔEx18}) and a severe early-onset syndrome characterized by epilepsy, global developmental delay, cognitive disabilities, and cerebellar atrophy. Using 2D neural differentiation and various 3D brain organoid models derived from patient iPSCs, we identified specific neurodevelopmental defects due to OXR1 depletion, including impairment of NPC proliferation, fate-specification, neurogenesis, neurite outgrowth, and neuronal migration. We revealed a role of OXR1 in epigenetic regulation of early human brain development by modulating PRMT-catalyzed histone arginine methylation.

The highly conserved TLDC domain is common for six different proteins (e.g., TBC1D24 and NCOA7), which all appear to display neuroprotective roles according to recent studies [3, 60]. A mutation in TBC1D24 was the first genetic cause of human epilepsy found [61]. Later, more than 50 mutations in TBC1D24 have been associated with various types of drug-resistant epilepsy, intellectual disability, and DOORS (deafness, onychodystrophy, osteodystrophy, mental retardation, and seizures) syndrome [62, 63]. Most pathogenic mutations of TBC1D24 are in the TBC domain and around 12 mutations are located in TLDC domain. Depletion of TBC1D24 by the acute silencing or mutation leads to defects in axon formation and maturation, and neuronal radial migration [64, 65], consistent with our finding that the OXR1 deficiency impaired axon

development (Figs. 3g, S3j, 5b, c). Interestingly, acute silencing of TBC1D24 in vivo showed reduced corpus callosum projections in rats [64], which was one of MRI signs identified in our OXR1 deficient patients.

Previous studies show that loss of OXR1 in various animal models and cell lines leads to neurodegeneration [3–5, 12, 17–20, 28]. Most of these studies demonstrate that the TLDC domain is essential for protection of neurons against oxidative and nitrosative stress-induced cell death, e.g. in mice cerebellum [3, 5, 12, 19, 23]. Other studies suggest that OXR1 could regulate glucose metabolism in mice cerebellum [23] or lysosomal structure and function in *Drosophila* neurons [4]. Here, we found elevated oxidative stress and increased cell apoptosis in human *OXR1*^{ΔEx18} patient derived lymphoblasts and 2D differentiated neurons (Additional file 1: Fig. S3i, k), which are the first human cell based models with minimal artificial intervention showing phenotypes due to OXR1 deficiency. In addition, we performed the deeper module analysis of enriched biological processes and identified the impaired mitochondrial function, glycolysis and autophagy in *OXR1*^{ΔEx18} neurons (Additional file 1: Fig. S3t). Oxidative eustress, also known as redox homeostasis is crucial for brain development [66]. We identified several key modulators of redox homeostasis that were significantly affected in Neu-*OXR1*^{ΔEx18}, including H₂O₂ scavengers, key redox-sensitive targets and redox hubs (Additional file 1: Fig. S3s,t), suggesting an important role of OXR1 not only in maintaining the balance between oxidative eustress and distress, but also in the proper redox signaling required for neuron development [66–69].

According to BrainSpan Atlas of the developing human brain [70], OXR1 expression increases largely from the early second trimester, reaching a plateau at two years of age until brain development is completed. OXR1 is highly expressed in neuronal cell types and is also detected in oligodendrocyte progenitor cells and microglia across human adult cortex (cited in <http://celltypes.brain-map.org/rnaseq>). Similarly, we detected an increased level of OXR1 during neural differentiation (Additional file 1: Fig. S3l). Both OXR1 deficient patients [4] and *OXR1* knockout mouse models [5, 12] showed cerebella related symptoms after birth. In lack of the access to viable human brain tissues, human brain organoids are the only models enabling advanced studies of brain development and patho-mechanisms. Importantly, brain organoids exhibit more complex cytoarchitecture over time including the organization of progenitor cells and sequential generation lamination of neurons. By using the 2D neural differentiation model, we found that OXR1-deficiency reduced neurite growth (Fig. 3a) as well as the expression of neuronal markers, e.g., MAP2 and Tuj1 (Additional file 1: Fig. S3i, j), suggesting an important role of OXR1 in neurodifferentiation. Taking the advantage of brain organoids in recapitulating the complexity of early corticogenesis, we revealed that OXR1 deficiency resulted in delay of specific cellular programs, including NPC proliferation, CP formation, cortical layering, and axon/dendrites growth. Cortical organoids at around day 50 coincide with the post-conception week (PCW) 14–16 in humans [71]. Impaired region-specific NPC proliferation and neurogenesis have been closely linked to primary microcephaly and vermis/cerebellar hypoplasia [72, 73]. We tried the protocol of cerebellum organoids described by the Sasai group [74]. Unfortunately, those organoids dissociated at an early stage, which limited our study of OXR1's roles in the cerebellar progenitor cell development and the maturation processes of cerebellar neuron subtypes. Efficient neural

induction, especially the application of region-specific patterning factors, restricts the generation of non-neuroectodermal cells (e.g., microglial, endothelial, and meningeal cells) that are critical to the development and function of the human brain. Recently, there have been significant advancements and attempts to improve organoid longevity and maturity, enhance glial cell production, reconstitute microglia and vasculatures, and fuse multiple region-specific organoids. We believe that future improvements will allow organoids to faithfully recapitulate late gestational and early post-natal development. In addition, the current study is limited due to the use of unrelated healthy iPS cells as control. Although we particularly chose a female control to minimize gender affection, these control cells share some differences in age, genetic background, and other factors with the patient iPS cells. In order to precisely generate human rare disease models, illustrate translational relevance, and develop new therapeutic approaches, an isogenic control with the same genetic background is very important in iPS-derived disease modeling. For example, direct correction of OXR1 genetic mutation in patient iPS cells, using genome editing technology, is warranted in future studies.

Genes essential for neurogenesis, neurodifferentiation, axon guidance, and cell migration were significantly down-regulated in Neu-*OXR1*^{ΔEx18} (Fig. 3f-g). Consistently, most altered factors in the OXR1-deficient organoids showed a similar trend of differential expression in OXR1-deficient neurons of the 2D model. For example, down-regulation of *MAP2* ($\text{Log}_2\text{FC} = -3.00$) and *RELN* ($\text{Log}_2\text{FC} = -5.36$) was identified in *OXR1*^{ΔEx18} neurons ($\text{Padj} < 0.05$) as detected in *OXR1*^{ΔEx18} cerebral organoids (Fig. 5b, c). Reduced expression of *TBR1* was observed in *OXR1*^{ΔEx18} cerebral organoids (Fig. 5b), but the expression of *TBR1* was barely detected in the 2D neural differentiation model. Further, the expression level of *FOXA2* ($\text{Log}_2\text{FC} = -7.32$) and *EN2* ($\text{Log}_2\text{FC} = -7.80$) was strikingly decreased in *OXR1*^{ΔEx18} neurons, which is consistent with the sparse detection of FOXA2-positive progenitors and failed induction of EN2 in *OXR1*^{ΔEx18} midbrain organoids (Fig. 7b, d). Although the level of *tyrosine hydroxylase* (*TH*) showed a significant decrease ($\text{Log}_2\text{FC} = -2.83$) in *OXR1*^{ΔEx18} neurons (the 2D neural differentiation model), the guided *OXR1*^{ΔEx18} midbrain dopaminergic (mDA) cells showed an abnormal increase of TH at day 50. Of note, the 2D neural differentiation model and the guided 3D brain organoid model represent distinct processes of neurodevelopment. Our work highlights the important role of OXR1 in shaping transcription during early neurodevelopment.

Arginine methylation, a widespread post-translational modification catalyzed by PRMTs, plays key roles in epigenetic regulation and signal transduction influencing gene transcription, RNA metabolism and DNA damage response. Dysregulation of arginine methylations has been linked to pathomechanisms of several diseases, including neurodegeneration (i.e., PRMT1-ALS, PRMT5-PD), and muscular disorders [17, 41, 75, 76]. PRMT5-mediated H4R3me2 is involved in regulating proliferative neuroepithelium/neural progenitors in mouse cortex [77]. Conditional depletion of PRMT5 in the mouse CNS (from E10.5) results in early postnatal lethality with severe developmental defects, e.g., depletion of the external granular layer of the cerebellum, reduced thickness of the cortex with decreased neuronal cells in CP and SOX2/Ki67-positive proliferating NPCs in VZ/SVZ [78]. In this study, we used various human cell culture systems and revealed the regulation of histone arginine methylation by the interaction of OXR1 and PRMT5

in human brain development. We provided direct evidence that OXR1 promoted PRMT5-mediated histone arginine (e.g., H4R3) methylations (Fig. 4d). In 2D derived NSC-*OXR1*^{ΔEx18}, OXR1 deficiency led to dysregulation of multiple histone arginine methylations (e.g., H4R3me2s/2a, H3R2me2a, H3R17me2s/2a, H3K4me3, H3K9me3, and H3K27me3) (Fig. 4b), without affecting the levels of different PRMTs (Additional file 1: Fig. S4b). Strikingly, the H4R3me2s associated genes overlapped with 71% of the down-regulated genes in the normal neural differentiation, of which 63% of the genes were differentially expressed (up-regulated) in NSC-*OXR1*^{ΔEx18} (Fig. 4c). Interestingly, H4R3me2s showed a specific distribution in the cortical brain organoids with a low level in VZ/SVZ like structures and increased levels in developing neurons outside the progenitor zone (Fig. 6d), suggesting a regulatory role of H4R3me2s during neurogenesis and the establishment of the cortical plate. However, the distribution of H4R3me2s in the midbrain organoids was distinct from the cortical brain organoids, showing a high level in the VZ progenitor zone (Fig. 7e). Notably, dysregulation of H4R3me2s was identified in *OXR1*^{ΔEx18} cortical and midbrain organoids, (Figs. 6d and 7e). It has been demonstrated that brain organoids possess comparable transcriptomic profiles to specific stages of fetal brains, as well as similar regulation of epigenetic programs, e.g., histone modifications [79, 80]. Our work reveals that OXR1 impacts histone arginine modifications in the early stage of human cortical and midbrain development, suggesting an important molecular patho-mechanism underlying the neurodevelopmental defects in *OXR1*^{ΔEx18} patients.

Conclusions

Altogether, we presented the first evidence of molecular neuropathology underlying OXR1 deficiency associated cerebellar atrophy, neurodevelopmental impairment, and increased susceptibility to oxidative stress. We provided new insights into the roles of OXR1 in cell survival and neural differentiation. We used brain organoids to recapitulate the early brain developmental defects of *OXR1*^{ΔEx18} patients in the context of brain region-specific cyto-architectures, including impaired NPC proliferation, neuronal fate specification, axon formation and neuronal migration. We revealed an important role of OXR1 in the epigenetic regulation of early human brain development by modulating PRMT-catalyzed histone arginine methylations. This study provides new insights into pathological features and molecular underpinnings associated with OXR1 deficiency in patients.

Methods

Whole exome analysis

Exonic sequences were enriched in the DNA sample of patient II-6 using SureSelect Human All Exon 50 Mb Kit (Agilent Technologies, Santa Clara, California, USA). Sequences were determined by HiSeq2000 (Illumina, San Diego, California, USA) as 100-bp paired-end runs. Data analysis including read alignment and variant calling was performed by DNAnexus software (Palo Alto, California, USA) using the default parameters with the human genome assembly hg19 (GRCh37) as reference.

Cell cultures

Immortalized lymphoblast cell (LB) lines were generated from patient II-4's and healthy control's peripheral blood mononuclear cells transformed with Epstein-Barr virus (EBV) as described by Bernacki SH et al. [81], in the National Laboratory for the Genetics of Israeli Populations (NLGIP). The cells were cultured at 37 °C with 5% CO₂ in growth medium: RPMI 1640 medium with GlutaMAX™ (Gibco, Cat.61870–010), supplemented with 20% fetal bovine serum (FBS), 100 IU/mL penicillin and 100 µg/mL streptomycin. Fibroblast cells and U2OS were cultured at 37 °C with 5% CO₂ in growth medium: DMEM medium (Sigma-Aldrich, D6429) supplemented with 10% FBS. The trypan blue (0.4%, Invitrogen™) exclusion method is used to determine the number of viable cells present in a cell suspension. Cell counting was employed on the Countess® automated cell counter (Invitrogen™).

Plasmids and electroporation and cell sorting

The human cDNA of *OXR1A* ORF (NM_001198533) and the truncated variants of *OXR1A*, *OXR1A* ΔTLDC₁ (lacking 69 aa from the C-terminal) and *OXR1A* ΔTLDC₂ (lacking the TLDC domain) were synthesized by GeneScript. They were inserted into plasmid pET28b and fused with the Hisx6 Tag between the Nde I and BamH I sites to obtain pET28b-*OXR1A* and pET28b-*OXR1A* ΔTLDC plasmids. All the plasmids were verified by sequencing. The plasmids of pET28b-*OXR1A*, *OXR1A* ΔTLDC₁ and *OXR1A* ΔTLDC₂ were transformed into *E. coli* and further used for the purification of recombinant hOXR1 proteins by Ni-NTA and gel filtration columns.

Full length cDNA (NM_001198534) representing human *OXR1D*, synthesized by RT-PCR with mRNA from human HeLa cells, was clone in vector pEGFP-N1 and pEGFP-C1 with the GFP Tag between the Xho I and BamH I sites, to obtain pEGFP-N-*OXR1D* plasmids and pEGFP-C-*OXR1D*, respectively.

The pEGFP-C-*OXR1D* (pE-*OXR1D*) and The pEGFP-N2 (Vector) were transfected into patients' LB (*OXR1*^{ΔEx18}) by electroporation using a method modified from the patent (CN 103981218 A) (Wenting Hou, et al. Department of Biochemistry and Molecular Biology Peking University Health Science Center). LB-*OXR1*^{ΔEx18} in log phase growth were counted and harvested by centrifugation at 800 × g for 10 min at room temperature. After two washes with RPMI 1640 containing 10% FBS, the cells were resuspended in 37 °C RPMI 1640 (with 10% FBS) at 1 × 10⁷ cells/mL. 250 µL of cell suspension and 15 µg of pEGFP-c-*OXR1D* or 12.5 µg of pEGFP-N2 (Vector) were combined in a BTX 0.4 cm electroporation cuvette. Electroporation was done with ECM-830 (BTX®) at 210 V/pulse length = 30 ms/pulse = 1. Electroporated cells were transferred to 2 mL of pre-warmed culture medium (with 10% FBS) at 37 °C. The electroporated cells were allowed to grow in 5% CO₂ at 37 °C for 48 h(h) before cell sorting. Fluorescence-activated cell sorting (FACS) of EGFP-labeled LB were accomplished by FacsAria Iiu high speed sorter at Flow Cytometry Core Facility, Oslo university hospital. The sorted cells were cultured at 37 °C with 5% CO₂ in growth medium for two weeks. The expression level of *OXR1* was tested by real time qPCR.

RNA isolation, cDNA sequence and gene expression analysis by quantitative real-time polymerase chain reaction

Total RNA was isolated from patient and control samples using the RNeasy Kit (Qiagen) following the manufacturer's protocol. The quality of purified RNA was estimated on an Epoch Microplate Spectrophotometer (Bio-Tek). Sequencing of *OXR1* cDNA from lymphocytes cDNA was prepared from fresh lymphocytes of patient II-4 and control using Maxima™ 1st strand cDNA synthesis kit (Thermo Scientific) and amplified by PCR using Phusion High-Fidelity PCR Master Mix (Thermo Scientific). The PCR products were separated using 2% (w/v) agarose gel electrophoresis and their sequence determined by Sanger sequencing. Two-steps qPCR method was used to determine mRNA levels. First, the cDNA was generated from total RNA samples using the High-capacity cDNA reverse transcription kit (Applied Biosystem). Real-time PCR reactions were prepared using Power SYBR Green Master mix including about 3 ng cDNA in each reaction, and qPCR was performed in the StepOnePlus™ Real-Time PCR System (Applied Biosystem) with the standard cycle conditions: 95 °C for 10 min(min); 40 cycles at 94 °C for 15 s(s) and 65 °C for 30 s. Samples were measured in triplicates. *ACTIN-β* and *GAPDH* were used as internal standard, as indicated. Quantification was done using the comparative cycle threshold (CT) method of relative quantification (RQ), where RQ is the normalized signal level in a sample relative to the normalized signal level in the corresponding calibrator. The CT for the target gene was normalized to the CT for *GAPDH* or *ACTIN-β* in the same sample, giving ΔCT sample. The average ΔCT from cells' cDNA was used as the ΔCT calibrator for the calculation of $\Delta\Delta CT$. RQ is defined as $2^{-\Delta\Delta CT}$, where $\Delta\Delta CT = \Delta CT$ sample - ΔCT calibrator. Primers used to amplify target genes by qPCR are as follows:

HO-1 F (5'- AACTTTCAGAAGGGCCAGGT-3'), R (5'- CTGGGCTCTCCTTGT TGC-3'); *NRF2* F (5'- ACACGGTCCACAGCTCATC-3'), R (5'-TGTC AATCAAATCCA TGTCTG-3');

P21 F (5'- GGCGGGCTGCATCCA -3'), R (5'- AGTGGTGTCTCGGTGACA AAGTC-3');

OXR1 F (5'-TTATGGTACTGGAGAGACCTTTGTTTT-3'),

R (5'- AAAACATATTATCTCCTGTCCACTTAAAGAC -3');

FOS F (5'- GGGGCAAGGTGGAACAGTTA-3'), R (5'- GTCTGTCTCCGCTTGGAG TG -3');

c-JUN F (5'-GTGCCGAAAAGGAAGCTGG-3'), R (5'- CTGCGTTAGCATGAG TTGGC-3');

DUSP1 F (5'- GGATACGAAGCGTTTTTCGGC-3'), R (5'-GGCCACCCTGATCGTAGA GT-3');

CASP9 F (5'- TCTACGGCACAGATGGATGC -3'), R (5'- CATGGTCTTTCTGCTCCC CA -3');

NANOG F (5'- AATACCTCAGCCTCCAGCAGATG -3'),

R (5'- TCGTACACACCATTGCTATTCTTC -3');

OCT4 F (5'- GTACTCCTCGGTCCCTTTCC -3'), R (5'- CAAAACCCTGGCACAAA CT -3');

SOX2 F (5'- GGATAAGTACACGCTGCCCG -3'), R (5'- ATGTGCGCGTAACTG TCCAT -3');

ACTIN F (5'- GTTACAGGAAGTCCCTTGCCATCC -3'),
R (5'- CACCTCCCCTGTGTGGACTTGGG -3');
GAPDH F (5'- CCACATCGCTCAGACACCAT -3'), R (5'- GCGCCCAATACGACC
AAAT -3').

Western blot

Cell pellets were prepared using RIPA lysis buffer (150 mM NaCl, 50 mM Tris pH 7.5, 1 mM EDTA, 0.1% SDS, 0.5% Sodium deoxycholate, and 1% Triton X-100, 1 mM DTT and 1 × Protease Inhibitor Cocktail). The soluble protein extracts were separated by SDS-PAGE (4–15% mini-protein TGX precast gel, 12 or 15 well, BioRad) and transferred to a PVDF membrane (Trans-blot Turbo mini-Format 0.2 μM PVDF, cat.170–4156 by BIO-RAD). The membrane was blocked with 5% milk in PBS-T buffer (137 mM NaCl, 2.7 mM KCl, 4.3 mM Na₂PO₄, 1.4 mM KH₂PO₄, 0.1% Tween-20) for 4 h at room temperature following incubation with the indicated primary antibodies, overnight at 4 °C. For detection, membranes were incubated with secondary antibodies diluted in PBS-T buffer, except anti-GAPDH-HRP 1:5000 (Abcam Cat# ab9482, RRID:AB_307272). After washing 3 times with PBS-T buffer, the membrane was developed with ECL substrate (Super Signal West Fem to Maximum Sensitivity Substrate, by Thermo Scientific). The signals were detected by a BIO-RAD Imager and analyzed by Image Lab software. A list of antibodies used is provided in Additional file 3: Table S1.

Cell viability and apoptosis assay

The LB cells were plated in 6-well plates at 1 × 10⁶ cells/mL overnight. Then the cells were exposed to the indicated concentrations of H₂O₂ in fresh medium for 1 h and recovered for 24 h. After treatment, the cells were stained with propidium iodide (PI) and annexin V using Alexa Fluor 488 annexin V/Dead cell apoptosis kit (Invitrogen, Cat.V13245) according to the manufacturer's instruction. Analysis was performed via flow cytometry with BD Accuri C6 Sample software. At least 10,000 cells were analyzed for each sample.

TUNEL staining

Apoptotic cell death was determined by In Situ cell death detection kit (Merck, Cat#11,684,795,910) according to the manufacturer's instructions. Briefly, cells were fixed with 4% paraformaldehyde and permeabilized with 0.1% Triton X-100 and 0.1% sodium citrate for 15 min. After washing, 100 μL of TUNEL reaction mixture was added and incubated for 1 h at 37 °C. The cells were counterstained with 1 μg/mL DAPI (4',6'-diamidino-2-phenylindole). The positive cells were imaged using an EVOS fluorescence microscope and analyzed using ImageJ software.

Cellular general ROS measurement

The LBs in 6-well plates at 1 × 10⁶ cells/mL were incubated with 10 μM ROS probe CM-H₂DCFDA (chloromethyl dichlorodihydrofluorescein diacetate, acetyl ester, Invitrogen, cat. 6827) in phosphate buffered saline (PBS) at 37°C for 30 min, washed once by PBS and recovered in phenol red free medium for 20 min. Next, the cells were exposed to 0.75 mM H₂O₂ in phenol red free medium for 1 h. Then, the cells were spin down and

washed once with PBS, re-suspended in 0.5 mL cold PBS and kept on ice in dark. The fluorescence was measured using a BD Accuri™ C6 Cytometer.

HPLC–MS/MS analysis of 8-oxo(dG) in genomic DNA

LBs were plated in 6-well plates at 1×10^6 cells/mL overnight, and then exposed to the indicated concentrations of H₂O₂ in fresh medium and harvested after 1 h, 4 h and 6 h treatment. Total DNA was isolated from LB using the DNeasy Kit (Qiagen) according to the manufacturer's instructions. This assay consists of two independent experiments with technical triplicates (the first assay) or sextuplicates (the second assay).

For mass spectrometry analysis, genomic DNA was enzymatically hydrolyzed to deoxyribonucleosides by incubation for 40 min at 40 °C in a mixture of benzonase (Santa Cruz Biotechnology, sc-391121B), nuclease P1 from *Penicillium citrinum* (Sigma, N8630), and alkaline phosphatase from *E. coli* (Sigma Aldrich, P5931) in 10 mM ammonium acetate buffer pH 6.0 with 1 mM magnesium chloride. Proteineous contaminants were precipitated by addition of three volume equivalents of ice-cold acetonitrile and centrifugation at 16,000 g at 4°C for 40 min. Supernatants were collected and vacuum-dried at room temperature. The resulting residues were dissolved in water for HPLC–MS/MS quantification.

Chromatographic separation and mass spectrometry detection of 8-oxo(dG) was performed at room temperature using an Agilent 1290 Infinity II UHPLC system coupled with an Agilent 6495 Triple Quad (Agilent Technologies, Germany) and an Eclipse Plus C18 1.8 µm 150 × 2.1 mm i.d. column equipped with a guard column. The mobile phases used were: A (0.1% formic acid in water), and B (0.1% formic acid in methanol). Chromatographic separation started with 95% A and 5% B for 2.5 min; followed by linear gradients of: 0.5 min 5–13% B, 2.5 min 13–17% B, 1.5 min 45–65% B, 1.5 min 65–70% B, 1 min 70–5% B; 4 min re-equilibration with 5% B.

Chromatographic separation of unmodified nucleosides was performed using a Shimadzu Prominence LC-20AD HPLC system with an Ascentis Express C18 2.7 µm 150 × 2.1 mm i.d. column equipped with an Ascentis Express Cartridge Guard Column (Supelco Analytical, Bellefonte, PA, USA) with EXP Titanium Hybrid Ferrule (Optimize Technologies Inc.). Chromatographic separation was performed with isocratic flow of 25% methanol in water with 0.1% formic acid, 0.16 ml/min at 40 °C. Online mass spectrometry detection of unmodified nucleosides was performed using an Applied Biosystems/MDS Sciex API5000 Triple quadrupole mass spectrometer (ABSciex, Toronto, Canada).

The deoxyribonucleosides were monitored by multiple reaction monitoring in positive electrospray ionization mode, using following mass transitions: 252.1 → 136.1 (dA), 228.1/112.1 (dC), 268.1/152.1 (dG), 243.1/127.0 (dT), 284.1/168.0 (8-oxodG).

mtDNA mutation frequency measurement

Total DNA containing nuclear DNA and mtDNA were isolated from LB using the DNeasy Kit (Qiagen) according to the manufacturer's instructions. Double stranded mtDNA mutation frequency was estimated as described previously [36]. Total DNA was digested with S1 nuclease (10U, Qiagen) for 15 min at 37 °C and subsequently digested with TaqI restriction enzyme (100U, New England Biolabs) at 65 °C for 1 h to remove

single strands, damaged DNA and non-mutated DNA. The remaining mutated TaqI restriction fragments were quantified in a qPCR reaction. To ensure complete digestion of non-mutated TaqI restriction sites, TaqI was added to qPCR reaction mixture (100 U) and an additional step of 65 °C for 15 min is included prior to the standard qPCR program. Mutation frequency is calculated as $(2^{\exp(\text{CT}_{\text{TaqI}} - \text{CT}_{\text{NT}})*4}) - 1$ per nt. The primer pairs for each gene were *I2S* F (5'- AAAGTGGCTCGCCAGAACAAC -3') and R (5'- CATGGGCTACACCTTGACCT -3'); *D loop* F (5'- CCCGGAGCGAGGAGAGTAG -3') and R (5'- CACCATCCTCCGTGAAATCAA -3').

Generation of human induced pluripotent stem cells (hiPSCs)

Fibroblasts from skin biopsy of patient II-2 and healthy control AG05836 (Coriell Institute) were cultured at 37 °C with 5% CO₂ in growth medium: DMEM medium, supplemented with 10% fetal calf serum, 100 IU/mL penicillin and 100 µg/mL streptomycin. iPSCs were generated with CytoTune[®]-iPS 2.0 Sendai Reprogramming Kit (ThermoFisher Scientific, Cat#A16517) using a multiplicity of infection of 5:5:3 (KOS:c-Myc:Klf4). Individual colonies with typical morphology of human embryonic stem cells were manually picked around 3–4 weeks after infection. The iPSCs were continuously cultured and expanded on Geltrex coated 6-well plates with Essential 8 medium (ThermoFisher Scientific, Cat#A1517001). Human iPSC cell lines used in this manuscript: AG05836 clone 1, 10, 15, 27 as healthy controls and OXR1 clone 2, 10, and 11.

Neural differentiation of hiPSCs

Differentiation of hiPSC towards neural lineage was performed as previously reported with modifications [82]. Briefly, iPSCs were pretreated with 50 µM Y-27632 (Stemcell Technologies) for 1 h. Then the cells were dissociated with Accutase (Stemcell Technologies) and plated onto low attachment V-type 96-well plate at 20 000 cells per well or AggreWell800 plate (Stemcell Technologies) to form aggregates. The culture was maintained in neural induction medium consisting of DMEM/F12 supplemented with 2% B27 supplement without vitamin A, 1% N2 supplement, 200 nM Noggin (R&D Systems) and 10 µM Y-27632 for 48 h. Formed aggregates were then transferred onto low attachment 6-well plates and continued culture for another 4 days. To induce neural rosette formation, the aggregates were transferred onto Geltrex coated 6-well plate and cultured for 4 days in neural induction medium supplemented with 200 ng/mL Noggin, 200 ng/mL DKK1 (R&D Systems), and 20 ng/mL bFGF (Life Technologies). Neural rosettes were manually picked and transferred onto low attachment 6-well plate in neural induction medium supplemented with 10 ng/mL bFGF and 10 ng/mL EGF to allow neuroepithelial sphere formation. Five days later, two procedures were performed to directly neural differentiation. First, the neural aggregates were placed onto Geltrex coated plates and treated with neural differentiation medium consisting of Neurobasal A medium supplemented with 10 ng/mL BDNF, 10 ng/mL GDNF, 200 µM ascorbic acid, 500 µM cyclic AMP. Second, the neural aggregates were dissociated into single cells with Accutase and replated onto poly-D-lysine/laminin coated 24 or 48-well plates for further differentiation with neural differentiation medium supplemented with 10 ng/mL BDNF, 10 ng/mL GDNF, 200 µM ascorbic acid, 500 µM cyclic AMP.

Generation of cerebral organoids

Generation of cerebral organoids from iPSCs was performed based on an unguided approach previously described [43] with minor modifications to improve reproducibility, especially batch variations. Briefly, the neuroectodermal in the form of neuronal rosette were generated from multipotent iPSC aggregates (EBs) in suspension using minimalistic media, coupled with Matrigel embedding, and followed by the expansion of the elaborate architecture of the germinal zone of neural stem cells or progenitor cells with the differentiated neurons migration outwards containing the neural tissues of diverse identities or the potential to developing into multiple neural structures. Neuroepithelial buds developed further in a bioreactor. A major modification was using pipetting technic to remove all debris accumulated around the EBs by setting a multichannel pipette at 30 μL and gently pipetting up and down 5 times just before half medium replacement, which, we found, could largely improve EB's quality. Another modification was to maintain the organoids in 96-well U-bottom ultra-low attachment plates until Matrigel embedding with half medium changing daily, aiming for individual organoid tracing and quality control.

Generation of brain region-specific organoids

Generation of brain region-specific organoids from iPSCs was performed mainly based on a previous report [44] with modifications. The major modifications include: 1) culturing iPSCs with feeder free methods and generating EBs with Aggrewell™ 800 plates; 2) patterning since Day1; and 3) three-dimensional suspension culturing on an orbital shaker (Thermo fisher) with 120 rpm since Day2. Briefly, on Day 0, iPSC colonies were detached from Matrigel (Corning, cat. no. 354230) and disassociated by ReLeSR™ (Stemcell Technologies). After washed with fresh stem cell medium with 10 μM Y-27632, 10,000 cells per microwell of Aggrewell™800 (3.0×10^6 per well of 24-well in 2 mL stem cell medium with 10 μM Y-27632) were seeded by centrifuging. From Day 1, half of the medium was replaced following protocols diverge for the procedures to differentiate forebrain, midbrain and hypothalamus organoids developed by Qian et al. [83]. The protocol of hippocampus organoids was developed by Fadi et al. [45]. Briefly on Day 2, around 30 organoids were transfer to each well of a 6-well plate placed on an orbital shaker rotating at 120 rpm in an incubator. For hippocampus organoids, on Days 1-7, half medium was replaced with EB medium consisting of DMEM/F12 (Thermo Fisher Scientific), 1X GlutaMAX™ Supplement(Thermo Fisher Scientific), 20% (vol/vol) KnockOut™ Serum Replacement (Thermo Fisher Scientific), 1X Antibiotic–Antimycotic (Thermo Fisher Scientific), 1X 2-Mercaptoethanol (Thermo Fisher Scientific), 1X Non-essential Amino Acids(NEAA, Thermo Fisher Scientific), 1 IU/mL Heparin (StemCell Technologies), 100 nM LDN193189 (StemCell Technologies), and 5 μM SB431542 (StemCell Technologies). On Days 8-14, medium was exchanged to hippocampus patterning medium consisting of DMEM/F12, 1X GlutaMAX™ Supplement, 1XNEAA, 1X N2 (Thermo Fisher Scientific), 1 IU/mL Heparin, 2 μM CHIR99021 (StemCell Technologies), and 10 ng/mL Recombinant Human BMP-7(Peprotech). On Days15-44, hippocampus neurogenesis medium was applied, which consists of 1:1 DMEM/F12: Neurobasal Medium (Thermo Fisher Scientific), 1X GlutaMAX™ Supplement, 1X NEAA, 1X N2, 1 IU/mL Heparin, 1X B-27 Supplement Minus Vitamin A, and 2.5 mg/mL human insulin (Sigma-Aldrich). After Day 45, neurogenesis medium was exchanged with maturation medium consisting

of 1:1 DMEM/F12: Neurobasal Medium, 1X GlutaMAX™ Supplement, 1X NEAA, 1X N2, 1 IU/mL Heparin, 1X B-27 Supplement Minus Vitamin A, 2.5 mg/mL human insulin, 20 ng/mL BDNF(Peprotech), 20 ng/mL recombinant Human GDNF (Peprotech), 200 µM Ascorbic Acid (StemCell Technologies), and 500 µM Dibutyryl-cAMP (Stem-Cell Technologies).

Immunofluorescent staining

Immunofluorescent staining of neural cells were performed as previously described [84]. The cells were fixed with 4% paraformaldehyde (PFA) for 15 min, permeabilized with 0.1% Triton-X100 in PBS for 15 min and blocked with 5% bovine serum albumin(BSA), 5% normal goat serum, and 0.1% Triton X-100 in PBS at room temperature for 30 min, then incubated with primary antibodies overnight at 4 °C. After washing with 0.1% Tween-20/PBS, the samples were incubated with secondary antibodies for 1 h and counterstained with DAPI nuclear staining. Quantitative results were obtained with ImageJ software counting 10 random fields of each experiment.

Brain organoids were fixed with 4% PFA for 30 min at room temperature. Organoids were washed 3 times with PBS and immersed in a sucrose solution gradient, 10% for 30 min, 20% for 1 h, then in 30% sucrose solution overnight. Organoids were embedded in tissue freezing medium (Tissue-Tek® O.C.T. Compound) and sectioned with a cryostat (Thermo) at 16 µm thickness. For immunostaining, cryosection slides were laid at room temperature for at least 20 min, washed 3 times with PBS before being blocked with blocking medium consisting of 5% goat serum, 5% bovine serum albumin, 0.5% Triton-X in PBS for 1 h followed by incubation with primary antibodies diluted in PBS buffer containing 0.5% goat serum, 0.5% BSA, 0.1% Tween 20 and 0.05% Triton-X at 4 °C overnight. For OXR1 staining, sections were then incubated at 90 °C in citrate antigen-retrieval buffer (pH 6.0) for 25 min and rinse once with PBS before blocking. After three washes in PBS containing 0.1% Tween 20, staining with secondary antibodies and DAPI was performed for 1 h at room temperature in the dark moisture chamber. After three washes in PBS containing 0.1% Tween 20 (10 min each), once quickly rinsing in PBS, and once quickly rinsing in pure water, the slides were mounted with ProLong™ Glass Antifade Mountant (Fisher Scientific, Waltham, Massachusetts). Cover glass thickness was 0.17 mm. The primary and secondary antibodies used, as well as their dilution are provided in Additional file 3: Table S1.

Analysis of immunolabelling

Images were captured on a Leica SP8 confocal microscope, using a 40 × oil-immersion objective. Image analysis was performed in Fiji (ImageJ, NIH). Prior to analysis, Z-stacks were flattened with maximum or average z-projection. The same capture conditions and analysis settings were applied on both control and patient organoid sections. For quantification of progenitor cell proliferation and apoptosis, organoids were stained for KI67 and cleaved Caspase3(cCas3), respectively. Random fan-shaped regions from the apical surfaces of the ventricular zone (VZ) to the boundary between the outer subventricular zone (oSVZ) and cortical plate (CP) or between VZ and intermediate zone (IZ) in midbrain organoids were cropped for analyses. KI67⁺ nuclei and cCas3⁺ were counted and divided by the total number of nuclei

stained by DAPI in the region respectively. To quantify the distribution of histone modifications in the developing cortical and midbrain organoids, radial structures were chosen randomly. From the pial surface to the basal surface, radial columns were cropped and evenly divided into 10–11 bins for analyses. The relative vertical position coordinates, y -coordinates on the image were recorded and normalized to the full thickness to measure their relative laminar positions in the differentiation and migration processes of midbrain progenitor cells or cortical laminar positions. The positions of each modification positive nuclei were separately marked using the Cell Counter plugin in Fuji(version 2.3.0). The positive cell proportion of the relative vertical positions in 10–11 evenly divided bins for each marker were calculated by (positive cell counts within each bin/total positive cell counts) and plotted in Prism (GraphPad 8.0). The mean intensity per cell were used to analysis the expression level of each marker.

RNA sequencing and analysis

We conducted RNA-sequencing with three individual clones of each genotype at three stages of neuronal differentiation: iPSC (iPS_CTRL and iPS_OXRI^{ΔEx18}), neural aggregate (NA) (NA_CTRL and NA_OXRI^{ΔEx18}), and neuron (Neu) (Neu_CTRL and Neu_OXRI^{ΔEx18}). in total, 18 samples were sequenced. Library construction and sequencing were performed through a commercially available service provided by BGI TECH SOLUTIONS (HONGKONG) CO. (Agreement No. F20FTSEUHT0295).

The quality control of fastq files was performed with FastQC v0.11.9 [85]. Alignment to reference genome (GRCh38) was accomplished with hisat2 v2.1.0 [86], while annotation and count matrix were computed with featureCounts v.2.0.0 [87]. We accomplished downstream DEGs analysis in R v3.6.1 with DESeq2 v1.24.0 [88]. Gene Set Enrichment Analysis(GSEA) [89] was performed to identify enriched pathways (using KEGG [90] and Reactome [91] databases) and gene ontology (GO) terms. Heatmaps were generated in R v3.6.1 with heatmap3 v1.1.7 [92]. For the topologic biological network analysis, 1978 leading-edge genes determined by GSEA, which contributed the most to the top enriched GO terms in nervous system development, cell adhesion, extracellular matrix organization, neuron death, stress response, mitochondrial genome maintenance, glucose metabolism, lysosomal structure, and TFs from DEGs with $|\text{Log}_2\text{FC}| > 0.5$ were recruited. Next, we constructed the protein–protein interaction (PPI) network for differential expression gene by searching STRING protein interaction database [93], with string score > 700 as the low limit value of confidence, $\text{FDR} < 5\%$, and then performed network modules analysis by ReactomeFIViz [91]. A topologic biological network composed of the PPIs of 1539 DEGs clustering into 44 modules were established to help us infer the central transcriptome events. Each module consists of a set of genes that are both connected in the protein functional interaction network and highly-correlated in biological databases [94]. We run cytoHubba [95], TRRUST [96] and iRegulon(v1.3) [97] to identify hub genes, the drivers of a module and highly connected, and the essential upstream regulators. This network data were imported into and visualized by Cytoscape software v3.8.1 [98].

Proximity ligation assay

Proximity ligation assays (PLAs) were performed on fibroblast cells derived from the *OXR1*^{ΔEx18} patient and a healthy control. Cells were grown on glass coverslips, fixed with 4% PFA (added 1 M glycine in the second wash step after fixation), and permeabilized with 0.1% Triton-X/1X PBS for 20 min. The PLA was conducted according to the manufacturer's instructions using the Duolink In Situ Red Starter Kit Mouse/Rabbit (Cat. No. DUO92101, SIGMA). After blocking for 30 min at 37 °C, the cells were incubated with anti-OXR1 (1:200) and PRMT5 antibody (1:200) or anti-OXR1 and anti-PRMT1 antibody (1:200) overnight at 4 °C. PLA Anti-Rabbit PLUS and Anti-Mouse MINUS probes containing the secondary antibodies conjugated with oligonucleotides, were added, and incubated at 37 °C for ligation 30 min. Then the fluorescently labeled oligonucleotides resulting in red fluorescence signals were added to the reaction and incubated for amplification at 37 °C for 100 min in the dark. The slides were mounted with Duolink In Situ Mounting Medium with DAPI (Cat. No. DUO82040, SIGMA). Microscopy was carried out using a Leica SP8 confocal microscope equipped with a 40X oil-immersion lens. The same input parameters were used throughout all experiments. Sample images were prepared in FUJI (ImageJ, NIH).

Immunoprecipitation assays

The U2OS cell pellet was lysed with NETN buffer (20 mM Tris-HCl pH 8.0, 100 mM NaCl, 0.5% NP-40, 0.5 mM DTT, 1:100 protease inhibitor cocktail, 400 U/mL). The lysate was pre-cleared by Dynabeads™ Protein A (ThermoFisher Scientific, Cat#10001D) beads for 30 min. 1 mg pre-clear cell lysate was pre-incubated with 1 μg of purified rabbit anti IgG antibody (Sigma-Aldrich Cat# I5006, RRID:AB_1163659) or 3 μg OXR1 antibody (Bethyl Cat# A302-036A, RRID:AB_1576565) for 1 h at 4°C rotator, and then incubated with 20 μl of protein A beads overnight at 4 °C with gentle agitation. The beads were pelleted and washed 3 times in 1 × TBS buffer (50 mM Tris HCl pH 7.4, 150 mM NaCl, add 1 mM PMSF before used). The precipitated proteins were denatured in SDS loading buffer at 95 °C for 10 min and separated in 10% SDS-PAGE gels.

Methylation assays with H4 N-terminal tail (aa 1–21) peptides

In vitro methylation assays were performed as previously described [1]. In a 30 μL reaction, 7.35 nM PRMT5/MEP50 complex (Active motif, Cat#31,356), 0.4 mM N-terminal H4 peptides, H4(1–21) WT and H4(1-21_R3K), with and without OXR1A or truncated OXR1A_ΔTLDC_1 or OXR1A_ΔTLDC_2, in a concentration gradient 1.83 nM(+), 7.35 nM(++) and 29.4 nM(+++) respectively, were carried out in 50 mM HEPES (pH 8.0), 10 mM NaCl, and 1 mM DTT containing [3H] SAM (25:1 molar ratio of SAM(NEB, Cat#B9003S) to [methyl-3H]-SAM (PerkinElmer, Cat#NET155001MC). Reactions were incubated for 1 h at 37°C, and then quenched with 0.5 μL of 100% trifluoroacetic acid. Each reaction was run in quadruplicate. Twenty-five microliters of each reaction were transferred to Merck Millipore MultiScreenHTS 96-Well Filter Plates with Negatively Charged Membrane (Cat#10,245,703) and air-dried for 30 min. The papers were subsequently washed in 50 mM NaHCO₃ at pH 9.0 for 45 min, then air dried. Radioactivity was counted using

1450 MicroBeta Instrument (Wallac at Department of Immunology and Transfusion Medicine, Oslo University Hospital, Oslo, Norway).

Quantification and statistical analysis

Each assay consists of at least two independent experiments with technical triplicates as described specifically. Data are presented as mean \pm S.E.M., or mean \pm S.D., as indicated in the figure legends. Organoid samples were randomly taken from the culture for experiments and analyses. Data analyses comparing control and OXR1 patient derived organoids were not performed blindly because the visual difference between the two groups is striking, and blinding was not possible to an informed researcher. Briefly, statistical analyses were performed using the *t* test in Excel or Graphpad Prism 8. A confidence level of 95% (* $p < 0.05$; ** $p < 0.01$, *** $p < 0.001$) was considered statistically significant. Detailed information was included in each figure legend.

Supplementary Information

The online version contains supplementary material available at <https://doi.org/10.1186/s13059-023-03037-1>.

Additional file 1. Supplementary Figures and Figure Legends.

Additional file 2. Supplementary Video 1, The cardiomyocyte differentiation of control (Video S1a) and OXR1^{ΔEx18} (Video S1b) iPSCs.

Additional file 3. Antibody List.

Additional file 4. Uncropped gel and microscopy images.

Additional file 5. Peer review history.

Acknowledgements

We thank the family of the described patients for participating in our studies.

Review history

The review history is available as Additional file 5.

Peer review information

Tim Sands was the primary editor of this article and managed its editorial process and peer review in collaboration with the rest of the editorial team.

Authors' contributions

XL, WW, MB, ND, MY and OE were responsible for concept and design of the study and involved in all aspects of the project. OE collect clinical information and generated lymphoblast and fibroblast cell lines from OXR1 patients and their healthy siblings. XL and MY performed experiments with LBs. AK and GS provided the 8-oxoG measurements in LBs genomic DNA. WW and GJS generated iPSC cell lines. WW and XL performed 2D neuronal differentiation experiments. MP and XL carried out RNA-seq analysis. XL and WW performed brain organoid experiments. F.J., H.S., G-I.M. contributed to brain organoid studies. MB and XL performed the methyltransferase assay. AARI, RS, and LE performed clinical data collection. MS, MAA, BAL, SE, and OE conducted clinical examination. XL, WW, JY, GJS, MMLS, BVL, SOB, WT, JEH, OE, AL, SE and MB wrote the initial manuscript. XL, JY and MB revised the manuscript. All authors reviewed the manuscript and approved the final version.

Funding

Open access funding provided by University of Oslo (incl Oslo University Hospital). Funding was provided by the Research Council of Norway, South-East Norway Regional Health Authority and Central Region Norway Health Authority. The Proteomics and Metabolomics Core Facility PROMEC is funded by NTNU and the Central Norway Regional Health Authority and is a member of the National Network of Advanced Proteomics Infrastructure (NAPI), which is funded by the RCN INFRASTRUKTUR-program (295910).

Availability of data and materials

Datasets supporting the conclusions are available in the Gene Expression Omnibus repository (GEO) at accession number (GSE:206,614) [99].

Declarations

Ethics approval and consent to participate

The study was performed with the approvals of the ethical committees of Hadassah Medical Center and the Ministry of Health (0393–17-HMO), and South-East Health Authorities of Norway (2014/658).

Competing interests

The authors declare no conflicts of interest.

Author details

¹Department of Microbiology, Oslo University Hospital and University of Oslo, Oslo, Norway. ²Department of Biochemistry, Oslo University Hospital and University of Oslo, Oslo, Norway. ³Department of Clinical and Molecular Medicine (IKOM), Norwegian University of Science and Technology (NTNU), 7491 Trondheim, Norway. ⁴Centre for Embryology and Healthy Development, University of Oslo and Oslo University Hospital, 0373 Oslo, Norway. ⁵Norwegian Centre for Stem Cell Research, Oslo University Hospital and University of Oslo, Oslo, Norway. ⁶Department of Pediatrics, Makassed Hospital and Al-Quds University, East Jerusalem, Palestine. ⁷Department of Neuroscience and Mahoney Institute for Neurosciences, University of Pennsylvania, Philadelphia, PA 19104, USA. ⁸Department of Pediatric Research, Oslo University Hospital and University of Oslo, Oslo, Norway. ⁹The Proteomics and Metabolomics Core Facility (PROMEC), Norwegian University of Science and Technology (NTNU), 7491 Trondheim, Norway. ¹⁰Department of Molecular Medicine, University of Oslo, Oslo, Norway. ¹¹Department of Newborn and Developmental Paediatrics, Toronto, ON, Canada. ¹²Department of Genetics, Hadassah University Hospital, Jerusalem, Israel. ¹³Department of Immunology, Oslo University Hospital and University of Oslo, Oslo, Norway.

Received: 21 May 2022 Accepted: 4 July 2023

Published online: 29 September 2023

References

- Yang M, Lin X, Segers F, Suganthan R, Hildrestrand GA, Rinholm JE, Aas PA, Sousa MML, Holm S, Bolstad N, et al. OXR1A, a Coactivator of PRMT5 Regulating Histone Arginine Methylation. *Cell Rep.* 2020;30:4165–4178 e4167.
- Blaise M, Alsarraf HM, Wong JE, Midtgaard SR, Laroche F, Schack L, Spaink H, Stougaard J, Thirup S. Crystal structure of the TLDC domain of oxidation resistance protein 2 from zebrafish. *Proteins.* 2012;80:1694–8.
- Finelli MJ, Sanchez-Pulido L, Liu KX, Davies KE, Oliver PL. The Evolutionarily Conserved Tre2/Bub2/Cdc16 (TBC), Lysin Motif (LysM), Domain Catalytic (TLDC) Domain Is Neuroprotective against Oxidative Stress. *J Biol Chem.* 2016;291:2751–63.
- Wang J, Rousseau J, Kim E, Ehresmann S, Cheng YT, Duraine L, Zuo Z, Park YJ, Li-Kroeger D, Bi W, et al. Loss of Oxidation Resistance 1, OXR1, Is Associated with an Autosomal-Recessive Neurological Disease with Cerebellar Atrophy and Lysosomal Dysfunction. *Am J Hum Genet.* 2019;105:1237–53.
- Svistunova DM, Simon JN, Rembeza E, Crabtree M, Yue WW, Oliver PL, Finelli MJ. Oxidation resistance 1 regulates post-translational modifications of peroxiredoxin 2 in the cerebellum. *Free Radic Biol Med.* 2019;130:151–62.
- Murphy KC, Volkert MR. Structural/functional analysis of the human OXR1 protein: identification of exon 8 as the anti-oxidant encoding function. *BMC Mol Biol.* 2012;13:26.
- Volkert MR, Elliott NA, Housman DE. Functional genomics reveals a family of eukaryotic oxidation protection genes. *Proc Natl Acad Sci U S A.* 2000;97:14530–5.
- Elliott NA, Volkert MR. Stress induction and mitochondrial localization of Oxr1 proteins in yeast and humans. *Mol Cell Biol.* 2004;24:3180–7.
- Durand M, Kolpak A, Farrell T, Elliott NA, Shao W, Brown M, Volkert MR. The OXR domain defines a conserved family of eukaryotic oxidation resistance proteins. *BMC Cell Biol.* 2007;8:13.
- Natoli R, Provis J, Valter K, Stone J. Expression and role of the early-response gene Oxr1 in the hyperoxia-challenged mouse retina. *Invest Ophthalmol Vis Sci.* 2008;49:4561–7.
- Jaramillo-Gutierrez G, Molina-Cruz A, Kumar S, Barillas-Mury C. The *Anopheles gambiae* oxidation resistance 1 (OXR1) gene regulates expression of enzymes that detoxify reactive oxygen species. *PLoS One.* 2010;5: e11168.
- Oliver PL, Finelli MJ, Edwards B, Bitoun E, Butts DL, Becker EB, Cheeseman MT, Davies B, Davies KE. Oxr1 is essential for protection against oxidative stress-induced neurodegeneration. *PLoS Genet.* 2011;7:e1002338.
- Sanada Y, Asai S, Ikemoto A, Moriwaki T, Nakamura N, Miyaji M, Zhang-Akiyama QM. Oxidation resistance 1 is essential for protection against oxidative stress and participates in the regulation of aging in *Caenorhabditis elegans*. *Free Radic Res.* 2014;48:919–28.
- Yang M, Luna L, Sorbo JG, Alseth I, Johansen RF, Backe PH, Danbolt NC, Eide L, Bjoras M. Human OXR1 maintains mitochondrial DNA integrity and counteracts hydrogen peroxide-induced oxidative stress by regulating antioxidant pathways involving p21. *Free Radic Biol Med.* 2014;77:41–8.
- Yang M, Lin X, Rowe A, Rognes T, Eide L, Bjoras M. Transcriptome analysis of human OXR1 depleted cells reveals its role in regulating the p53 signaling pathway. *Sci Rep.* 2015;5:17409.
- Wu Y, Davies KE, Oliver PL. The antioxidant protein Oxr1 influences aspects of mitochondrial morphology. *Free Radic Biol Med.* 2016;95:255–67.
- Finelli MJ, Liu KX, Wu Y, Oliver PL, Davies KE. Oxr1 improves pathogenic cellular features of ALS-associated FUS and TDP-43 mutations. *Hum Mol Genet.* 2015;24:3529–44.
- Liu KX, Edwards B, Lee S, Finelli MJ, Davies B, Davies KE, Oliver PL. Neuron-specific antioxidant OXR1 extends survival of a mouse model of amyotrophic lateral sclerosis. *Brain.* 2015;138:1167–81.

19. Williamson MG, Finelli MJ, Sleigh JN, Reddington A, Gordon D, Talbot K, Davies KE, Oliver PL. Neuronal over-expression of Oxr1 is protective against ALS-associated mutant TDP-43 mislocalisation in motor neurons and neuromuscular defects in vivo. *Hum Mol Genet.* 2019;28:3584–99.
20. Jiang Y, Liu J, Chen L, Jin Y, Zhang G, Lin Z, Du S, Fu Z, Chen T, Qin Y, Sun X. Serum secreted miR-137-containing exosomes affects oxidative stress of neurons by regulating OXR1 in Parkinson's disease. *Brain Res.* 2019;1722:146331.
21. Dianat M, Radan M, Mard SA, Sohrabi F, Saryazdi SSN. Contribution of reactive oxygen species via the OXR1 signaling pathway in the pathogenesis of monocrotaline-induced pulmonary arterial hypertension: The protective role of Crocin. *Life Sci.* 2020;256:117848.
22. Matsui A, Hashiguchi K, Suzuki M, Zhang-Akiyama QM. Oxidation resistance 1 functions in the maintenance of cellular survival and genome stability in response to oxidative stress-independent DNA damage. *Genes Environ.* 2020;42:29.
23. Finelli MJ, Paramo T, Pires E, Ryan BJ, Wade-Martins R, Biggin PC, McCullagh J, Oliver PL. Oxidation Resistance 1 Modulates Glycolytic Pathways in the Cerebellum via an Interaction with Glucose-6-Phosphate Isomerase. *Mol Neurobiol.* 2019;56:1558–77.
24. Khan MM, Lee S, Couoh-Cardel S, Oot RA, Kim H, Wilkens S, Roh SH. Oxidative stress protein Oxr1 promotes V-ATPase holoenzyme disassembly in catalytic activity-independent manner. *EMBO J.* 2022;41:e109360.
25. Su LD, Zhang QL, Lu Z. Oxidation resistance 1 (OXR1) participates in silkworm defense against bacterial infection through the JNK pathway. *Insect Sci.* 2017;24:17–26.
26. Jardeleza C, Jones D, Baker L, Miljkovic D, Boase S, Tan NC, Vreugde S, Tan LW, Wormald PJ. Gene expression differences in nitric oxide and reactive oxygen species regulation point to an altered innate immune response in chronic rhinosinusitis. *Int Forum Allergy Rhinol.* 2013;3:193–8.
27. Li Y, Li W, Liu C, Yan M, Raman I, Du Y, Fang X, Zhou XJ, Mohan C, Li QZ. Delivering Oxidation Resistance-1 (OXR1) to Mouse Kidney by Genetic Modified Mesenchymal Stem Cells Exhibited Enhanced Protection against Nephrotoxic Serum Induced Renal Injury and Lupus Nephritis. *J Stem Cell Res Ther.* 2014;4(9):231.
28. Yang L, Shen Q, Xia Y, Lei X, Peng J. Sevoflurane-induced neurotoxicity is driven by OXR1 posttranscriptional down-regulation involving hsamiR302e. *Mol Med Rep.* 2018;18:4657–65.
29. Xu H, Jiang Y, Li S, Xie L, Tao YX, Li Y. Zebrafish Oxr1a Knockout Reveals Its Role in Regulating Antioxidant Defenses and Aging. *Genes (Basel).* 2020;11(10):1118.
30. Murray AR, Chen Q, Takahashi Y, Zhou KK, Park K, Ma JX. MicroRNA-200b downregulates oxidation resistance 1 (Oxr1) expression in the retina of type 1 diabetes model. *Invest Ophthalmol Vis Sci.* 2013;54:1689–97.
31. Sahu B, Leon LM, Zhang W, Puranik N, Periasamy R, Khanna H, Volkert M. Oxidative Stress Resistance 1 Gene Therapy Retards Neurodegeneration in the rd1 Mutant Mouse Model of Retinopathy. *Invest Ophthalmol Vis Sci.* 2021;62:8.
32. Zhou Y, Meng P, Tang B, Ke Z, Liu L, Chen Y, Zhu F. MiR-616 promotes the progression of pancreatic carcinoma by targeting OXR1. *Minerva Med.* 2021;112(4):528–9.
33. Wang L, Wang L, Chang W, Li Y, Wang L. MicroRNA-373 promotes the development of esophageal squamous cell carcinoma by targeting LATS2 and OXR1. *Int J Biol Markers.* 2019;34:148–55.
34. Massaad CA, Klann E. Reactive oxygen species in the regulation of synaptic plasticity and memory. *Antioxid Redox Signal.* 2011;14:2013–54.
35. Kanvah S, Joseph J, Schuster GB, Barnett RN, Cleveland CL, Landman U. Oxidation of DNA: damage to nucleobases. *Acc Chem Res.* 2010;43:280–7.
36. Wang W, Scheffler K, Esbensen Y, Strand JM, Stewart JB, Bjoras M, Eide L. Addressing RNA integrity to determine the impact of mitochondrial DNA mutations on brain mitochondrial function with age. *PLoS One.* 2014;9:e96940.
37. Arenas E, Denham M, Villaescusa JC. How to make a midbrain dopaminergic neuron. *Development.* 2015;142:1918–36.
38. Fothergill T, Donahoo AL, Douglass A, Zalucki O, Yuan J, Shu T, Goodhill GJ, Richards LJ. Netrin-DCC signaling regulates corpus callosum formation through attraction of pioneering axons and by modulating Slit2-mediated repulsion. *Cereb Cortex.* 2014;24:1138–51.
39. Piper M, Plachez C, Zalucki O, Fothergill T, Goudreau G, Erzurumlu R, Gu C, Richards LJ. Neuropilin 1-Sema signaling regulates crossing of cingulate pioneering axons during development of the corpus callosum. *Cereb Cortex.* 2009;19(Suppl 1):i11–21.
40. Hutchins BI, Li L, Kalil K. Wnt/calcium signaling mediates axon growth and guidance in the developing corpus callosum. *Dev Neurobiol.* 2011;71:269–83.
41. Blanc RS, Richard S. Arginine Methylation: The Coming of Age. *Mol Cell.* 2017;65:8–24.
42. Molina-Serrano D, Schiza V, Kirmizis A. Cross-talk among epigenetic modifications: lessons from histone arginine methylation. *Biochem Soc Trans.* 2013;41:751–9.
43. Lancaster MA, Knoblich JA. Generation of cerebral organoids from human pluripotent stem cells. *Nat Protoc.* 2014;9:2329–40.
44. Qian X, Jacob F, Song MM, Nguyen HN, Song H, Ming GL. Generation of human brain region-specific organoids using a miniaturized spinning bioreactor. *Nat Protoc.* 2018;13:565–80.
45. Jacob F, Pather SR, Huang WK, Zhang F, Wong SZH, Zhou H, Cubitt B, Fan W, Chen CZ, Xu M, et al. Human Pluripotent Stem Cell-Derived Neural Cells and Brain Organoids Reveal SARS-CoV-2 Neurotropism Predominates in Choroid Plexus Epithelium. *Cell Stem Cell.* 2020;27:937–950 e939.
46. Meyer G, Gonzalez-Gomez M. The heterogeneity of human Cajal-Retzius neurons. *Semin Cell Dev Biol.* 2018;76:101–11.
47. Stranahan AM, Erion JR, Wosiski-Kuhn M. Reelin signaling in development, maintenance, and plasticity of neural networks. *Ageing Res Rev.* 2013;12:815–22.
48. Qian X, Nguyen HN, Song MM, Hadiono C, Ogden SC, Hammack C, Yao B, Hamersky GR, Jacob F, Zhong C, et al. Brain-Region-Specific Organoids Using Mini-bioreactors for Modeling ZIKV Exposure. *Cell.* 2016;165:1238–54.

49. Jacob F, Pather SR, Huang WK, Wong SZH, Zhou H, Zhang F, Cubitt B, Chen CZ, Xu M, et al. Human Pluripotent Stem Cell-Derived Neural Cells and Brain Organoids Reveal SARS-CoV-2 Neurotropism. *Cell Stem Cell*. 2020;27(6):937–950. e9
50. Hayes L, Zhang Z, Albert P, Zervas M, Ahn S. Timing of Sonic hedgehog and Gli1 expression segregates midbrain dopamine neurons. *J Comp Neurol*. 2011;519:3001–18.
51. Blaess S, Bodea GO, Kabanova A, Chanet S, Mugniery E, Derouiche A, Stephen D, Joyner AL. Temporal-spatial changes in Sonic Hedgehog expression and signaling reveal different potentials of ventral mesencephalic progenitors to populate distinct ventral midbrain nuclei. *Neural Dev*. 2011;6:29.
52. Brown A, Machan JT, Hayes L, Zervas M. Molecular organization and timing of Wnt1 expression define cohorts of midbrain dopamine neuron progenitors in vivo. *J Comp Neurol*. 2011;519:2978–3000.
53. Yang J, Brown A, Ellisor D, Paul E, Hagan N, Zervas M. Dynamic temporal requirement of Wnt1 in midbrain dopamine neuron development. *Development*. 2013;140:1342–52.
54. Lin W, Metzakopian E, Mavromatakis YE, Gao N, Balaskas N, Sasaki H, Briscoe J, Whitsett JA, Goulding M, Kaestner KH, Ang SL. Foxa1 and Foxa2 function both upstream of and cooperatively with Lmx1a and Lmx1b in a feedforward loop promoting mesodiencephalic dopaminergic neuron development. *Dev Biol*. 2009;333:386–96.
55. Ono Y, Nakatani T, Sakamoto Y, Mizuhara E, Minaki Y, Kumai M, Hamaguchi A, Nishimura M, Inoue Y, Hayashi H, et al. Differences in neurogenic potential in floor plate cells along an anteroposterior location: midbrain dopaminergic neurons originate from mesencephalic floor plate cells. *Development*. 2007;134:3213–25.
56. Kriks S, Shim JW, Piao J, Ganat YM, Wakeman DR, Xie Z, Carrillo-Reid L, Auyeung G, Antonacci C, Buch A, et al. Dopamine neurons derived from human ES cells efficiently engraft in animal models of Parkinson's disease. *Nature*. 2011;480:547–51.
57. Haldipur P, Aldinger KA, Bernardo S, Deng M, Timms AE, Overman LM, Winter C, Lisgo SN, Razavi F, Silvestri E, et al. Spatiotemporal expansion of primary progenitor zones in the developing human cerebellum. *Science*. 2019;366:454–60.
58. Orvis GD, Hartzell AL, Smith JB, Barraza LH, Wilson SL, Szulc KU, Turnbull DH, Joyner AL. The engrailed homeobox genes are required in multiple cell lineages to coordinate sequential formation of fissures and growth of the cerebellum. *Dev Biol*. 2012;367:25–39.
59. Harada H, Sato T, Nakamura H. Fgf8 signaling for development of the midbrain and hindbrain. *Dev Growth Differ*. 2016;58:437–45.
60. Finelli MJ, Aprile D, Castroflorio E, Jeans A, Moschetta M, Chessum L, Degiacomi MT, Grassegger J, Lupien-Meilleur A, Bassett A, et al. The epilepsy-associated protein TBC1D24 is required for normal development, survival and vesicle trafficking in mammalian neurons. *Hum Mol Genet*. 2019;28:584–97.
61. Corbett MA, Bahlo M, Jolly L, Afawi Z, Gardner AE, Oliver KL, Tan S, Coffey A, Mulley JC, Dibbens LM, et al. A focal epilepsy and intellectual disability syndrome is due to a mutation in TBC1D24. *Am J Hum Genet*. 2010;87:371–5.
62. Balestrini S, Milh M, Castiglioni C, Luthy K, Finelli MJ, Verstreken P, Cardon A, Strazisar BG, Holder JL Jr, Lesca G, et al. TBC1D24 genotype-phenotype correlation: Epilepsies and other neurologic features. *Neurology*. 2016;87:77–85.
63. Luthy K, Mei D, Fischer B, De Fusco M, Swerts J, Paesmans J, Parrini E, Lubarr N, Meijer IA, Mackenzie KM, et al. TBC1D24-TLDC-related epilepsy exercise-induced dystonia: rescue by antioxidants in a disease model. *Brain*. 2019;142:2319–35.
64. Aprile D, Fruscione F, Baldassari S, Fadda M, Ferrante D, Falace A, Buhler E, Sartorelli J, Represa A, Baldelli P, et al. TBC1D24 regulates axonal outgrowth and membrane trafficking at the growth cone in rodent and human neurons. *Cell Death Differ*. 2019;26:2464–78.
65. Falace A, Filippello F, La Padula V, Vanni N, Madia F, De Pietri TD, de Falco FA, Striano P, Dagna Bricarelli F, Minetti C, et al. TBC1D24, an ARF6-interacting protein, is mutated in familial infantile myoclonic epilepsy. *Am J Hum Genet*. 2010;87:365–70.
66. Sies H, Jones DP. Reactive oxygen species (ROS) as pleiotropic physiological signalling agents. *Nat Rev Mol Cell Biol*. 2020;21:363–83.
67. Varadaraj K, Kumari SS. Lens aquaporins function as peroxiporins to facilitate membrane transport of hydrogen peroxide. *Biochem Biophys Res Commun*. 2020;524:1025–9.
68. Rhee SG, Kil IS. Multiple Functions and Regulation of Mammalian Peroxiredoxins. *Annu Rev Biochem*. 2017;86:749–75.
69. Brigelius-Flohe R, Flohe L. Regulatory Phenomena in the Glutathione Peroxidase Superfamily. *Antioxid Redox Signal*. 2020;33:498–516.
70. Miller JA, Ding SL, Sunkin SM, Smith KA, Ng L, Szafer A, Ebbert A, Riley ZL, Royall JJ, Aiona K, et al. Transcriptional landscape of the prenatal human brain. *Nature*. 2014;508:199–206.
71. Torres-Cuevas I, Parra-Llorca A, Sanchez-Illana A, Nunez-Ramiro A, Kuligowski J, Chafer-Pericas C, Cernada M, Escobar J, Vento M. Oxygen and oxidative stress in the perinatal period. *Redox Biol*. 2017;12:674–81.
72. Basson MA, Wingate RJ. Congenital hypoplasia of the cerebellum: developmental causes and behavioral consequences. *Front Neuroanat*. 2013;7:29.
73. Subramanian L, Calcagnotto ME, Paredes MF. Cortical Malformations: Lessons in Human Brain Development. *Front Cell Neurosci*. 2019;13:576.
74. Muguruma K, Nishiyama A, Kawakami H, Hashimoto K, Sasai Y. Self-organization of polarized cerebellar tissue in 3D culture of human pluripotent stem cells. *Cell Rep*. 2015;10:537–50.
75. Larsen SC, Sylvestersen KB, Mund A, Lyon D, Mullari M, Madsen MV, Daniel JA, Jensen LJ, Nielsen ML. Proteome-wide analysis of arginine monomethylation reveals widespread occurrence in human cells. *Sci Signal*. 2016;9:rs9.
76. Guccione E, Richard S. The regulation, functions and clinical relevance of arginine methylation. *Nat Rev Mol Cell Biol*. 2019;20:642–57.
77. Chittka A. Dynamic distribution of histone H4 arginine 3 methylation marks in the developing murine cortex. *PLoS One*. 2010;5:e13807.

78. Bezzi M, Teo SX, Muller J, Mok WC, Sahu SK, Vardy LA, Bonday ZQ, Guccione E. Regulation of constitutive and alternative splicing by PRMT5 reveals a role for Mdm4 pre-mRNA in sensing defects in the spliceosomal machinery. *Genes Dev.* 2013;27:1903–16.
79. Amiri A, Coppola G, Scuderi S, Wu F, Roychowdhury T, Liu F, Pochareddy S, Shin Y, Safi A, Song L, et al. Transcriptome and epigenome landscape of human cortical development modeled in organoids. *Science.* 2018;362(6420):eaat6720.
80. Trevino AE, Sinnott-Armstrong N, Andersen J, Yoon SJ, Huber N, Pritchard JK, Chang HY, Greenleaf WJ, Pasca SP. Chromatin accessibility dynamics in a model of human forebrain development. *Science.* 2020;367(6476):eaay1645.
81. Bernacki SH, Stankovic AK, Williams LO, Beck JC, Herndon JE, Snow-Bailey K, Prior TW, Matteson KJ, Wasserman LM, Cole EC, Stenzel TT. Establishment of stably EBV-transformed cell lines from residual clinical blood samples for use in performance evaluation and quality assurance in molecular genetic testing. *J Mol Diagn.* 2003;5:227–30.
82. Mariani J, Coppola G, Zhang P, Abyzov A, Provini L, Tomasini L, Amenduni M, Szekely A, Palejev D, Wilson M, et al. FOXP1-Dependent Dysregulation of GABA/Glutamate Neuron Differentiation in Autism Spectrum Disorders. *Cell.* 2015;162:375–90.
83. Qian X, Su Y, Adam CD, Deutschmann AU, Pather SR, Goldberg EM, Su K, Li S, Lu L, Jacob F, et al. Sliced Human Cortical Organoids for Modeling Distinct Cortical Layer Formation. *Cell Stem Cell.* 2020;26:766–781 e769.
84. Wang W, Esbensen Y, Kunke D, Suganthan R, Rachek L, Bjoras M, Eide L. Mitochondrial DNA damage level determines neural stem cell differentiation fate. *J Neurosci.* 2011;31:9746–51.
85. S. A: FastQC: a quality control tool for high throughput sequence data. 2010.
86. Kim D, Langmead B, Salzberg SL. HISAT: a fast spliced aligner with low memory requirements. *Nat Methods.* 2015;12:357–60.
87. Liao Y, Smyth GK, Shi W. featureCounts: an efficient general purpose program for assigning sequence reads to genomic features. *Bioinformatics.* 2014;30:923–30.
88. Love MI, Huber W, Anders S. Moderated estimation of fold change and dispersion for RNA-seq data with DESeq2. *Genome Biol.* 2014;15:550.
89. Subramanian A, Tamayo P, Mootha VK, Mukherjee S, Ebert BL, Gillette MA, Paulovich A, Pomeroy SL, Golub TR, Lander ES, Mesirov JP. Gene set enrichment analysis: a knowledge-based approach for interpreting genome-wide expression profiles. *Proc Natl Acad Sci U S A.* 2005;102:15545–50.
90. Kanehisa M, Goto S. KEGG: kyoto encyclopedia of genes and genomes. *Nucleic Acids Res.* 2000;28:27–30.
91. Jassal B, Matthews L, Viteri G, Gong C, Lorente P, Fabregat A, Sidiropoulos K, Cook J, Gillespie M, Haw R, et al. The reactome pathway knowledgebase. *Nucleic Acids Res.* 2020;48:D498–503.
92. Zhao S, Guo Y, Sheng Q, Shyr Y. Advanced heat map and clustering analysis using heatmap3. *Biomed Res Int.* 2014;2014:986048.
93. Szklarczyk D, Gable AL, Lyon D, Junge A, Wyder S, Huerta-Cepas J, Simonovic M, Doncheva NT, Morris JH, Bork P, et al. STRING v11: protein-protein association networks with increased coverage, supporting functional discovery in genome-wide experimental datasets. *Nucleic Acids Res.* 2019;47:D607–13.
94. Wu G, Dawson E, Duong A, Haw R, Stein L. ReactomeFIViz: a Cytoscape app for pathway and network-based data analysis. *F1000Res.* 2014;3:146.
95. Chin CH, Chen SH, Wu HH, Ho CW, Ko MT, Lin CY. cytoHubba: identifying hub objects and sub-networks from complex interactome. *BMC Syst Biol.* 2014;8(Suppl 4):S11.
96. Han H, Cho JW, Lee S, Yun A, Kim H, Bae D, Yang S, Kim CY, Lee M, Kim E, et al. TRRUST v2: an expanded reference database of human and mouse transcriptional regulatory interactions. *Nucleic Acids Res.* 2018;46:D380–6.
97. Janky R, Verfaillie A, Imrichova H, Van de Sande B, Standaert L, Christiaens V, Hulselmans G, Herten K, Naval Sanchez M, Potier D, et al. iRegulon: from a gene list to a gene regulatory network using large motif and track collections. *PLoS Comput Biol.* 2014;10:e1003731.
98. Shannon P, Markiel A, Ozier O, Baliga NS, Wang JT, Ramage D, Amin N, Schwikowski B, Ideker T. Cytoscape: a software environment for integrated models of biomolecular interaction networks. *Genome Res.* 2003;13:2498–504.
99. Lin X, Pannone M, Wang W, Yang M, Kristiansen E, Edvardson S, Ye J, Bjørås M. A loss-of-function mutation in human Oxidation Resistance 1 disrupts the spatial-temporal regulation of histone arginine methylation in neurodevelopment. *GEO: GSE206614.* (2023). <https://www.ncbi.nlm.nih.gov/geo/query/acc.cgi?acc=GSE206614>.

Publisher's Note

Springer Nature remains neutral with regard to jurisdictional claims in published maps and institutional affiliations.

Ready to submit your research? Choose BMC and benefit from:

- fast, convenient online submission
- thorough peer review by experienced researchers in your field
- rapid publication on acceptance
- support for research data, including large and complex data types
- gold Open Access which fosters wider collaboration and increased citations
- maximum visibility for your research: over 100M website views per year

At BMC, research is always in progress.

Learn more biomedcentral.com/submissions

